

# NETFORMER: AN INTERPRETABLE MODEL FOR RECOVERING DYNAMICAL CONNECTIVITY IN NEURONAL POPULATION DYNAMICS

**Anonymous authors**

Paper under double-blind review

## ABSTRACT

Neuronal dynamics are highly nonlinear and nonstationary. Traditional methods for extracting the underlying network structure from neuronal activity recordings mainly concentrate on modeling static connectivity, without accounting for key nonstationary aspects of biological neural systems, such as ongoing synaptic plasticity and neuronal modulation. To bridge this gap, we introduce the NetFormer model, an interpretable approach applicable to such systems. In NetFormer, the activity of each neuron across a series of historical time steps is defined as a token. These tokens are then linearly mapped through a query and key mechanism to generate a state- (and hence time-) dependent attention matrix that directly encodes nonstationary connectivity structures. We analyze our formulation from the perspective of nonstationary and nonlinear networked dynamical systems, and show both via an analytical expansion and targeted simulations how it can approximate the underlying ground truth. Next, we demonstrate NetFormer’s ability to model a key feature of biological networks, spike-timing-dependent plasticity, whereby connection strengths continually change in response to local activity patterns. *We further demonstrate that NetFormer can capture task-induced connectivity patterns on activity generated by task-trained recurrent neural networks.* Thus informed, we apply NetFormer to a multi-modal dataset of real neural recordings, which contains neural activity, cell type, and behavioral state information. We show that NetFormer effectively predicts neural dynamics and identifies cell-type specific, state-dependent dynamic connectivity that matches patterns measured in separate ground-truth physiology experiments, demonstrating its ability to help decode complex neural interactions based on population activity observations alone.

## 1 INTRODUCTION

Inferring the underlying connectivity of a network from observations of the activity of its units is a long-standing challenge. In the brain, this challenge is exacerbated by (i) different nonlinear dynamics present in individual neurons, (ii) the difficulty of experimentally sampling the full neuronal population simultaneously, and (iii) dynamic reconfiguration of effective connectivity, mediated by both synaptic plasticity and neuromodulation. This last issue carries significant practical importance in studying behavioral dynamics, learning and memory (Bargmann, 2012; Tyulmankov et al., 2021; Marder, 2012; Liu et al., 2021; Aitken & Mihalas, 2023). As such, it poses a (harder) generalization of the classical problem where the connectivity should no longer be considered as a static unknown, rather as a dynamical variable that needs to be inferred and tracked over time.

A surrogate, but not sufficient, measure of success in unsupervised inference of connectivity is the inferred network’s success in fitting the observed dynamics. While traditional linear dynamical models struggle to capture the essential nonlinear mechanisms of leaky integration and firing (Gerstner & Kistler, 2002) in biological neurons, more sophisticated nonlinear models typically suffer from a lack of interpretability, making it difficult to identify the underlying connectivity (Pandarinath et al., 2018; Le & Shlizerman, 2022; Ye et al., 2023). Moreover, traditional approaches often adopt a static perspective on connectivity (Tank et al., 2021; Löwe et al., 2022), failing to account for the nonstationary interactions, such as those produced by plasticity and modulation at synapses.

054 Here we propose an interpretable nonlinear and nonstationary dynamical model to represent inter-  
055 actions between neurons (Figure 1), based on the fast weight programming nature of the attention  
056 mechanism (Schlag et al., 2021). Prior research has suggested that the attention mechanism can reveal  
057 information about the underlying structure of a system (Singh & Buckley, 2023; Lu et al., 2023).  
058 We further removed the softmax activation function in the attention mechanism, as the constraint of  
059 attention weights summing up to one is not biologically meaningful because neither the in-degrees  
060 nor the out-degrees of neuronal connectivity (nor their counterparts incorporating synaptic strength)  
061 are invariant across neurons (Santuy et al., 2020). We first demonstrated with both mathematical  
062 analysis and simulation study that even without the softmax activation, the core part of the attention  
063 mechanism – the dot-product between queries and keys – is capable of capturing nonstationary and  
064 nonlinear structural information. Next, we applied this novel approach to a wide range of simulated  
065 networks including nonstationary and/or complex nonlinear connectivity patterns, and showed that  
066 it can recover ground truth connectivity information. We then applied it to a large-scale, publicly  
067 available dataset of neuronal activity recordings. Importantly, this dataset includes the genetic *cell*  
068 *type* of individual neurons, enabling us to compare our predictions for cell-type level connectivity  
069 patterns against known ground truth values from independent experiments. Taken together, this  
070 shows the potential of our method for recovering interpretable connectivity information, even in the  
071 presence of complex nonlinear and nonstationary network dynamics.

072 Our main contributions are as follows: (i) We formulated a **transformer**-inspired **network** model,  
073 the NetFormer, for which the core of the attention mechanism – the dot-product between queries  
074 and keys – directly encodes nonstationary and nonlinear structure of networks; (ii) On a simulated  
075 network with the spike-timing-dependent plasticity mechanism, we demonstrated that the inferred  
076 time-varying weights from attention aligned with the underlying changes in connectivity; (iii) *On*  
077 *activity generated by task-trained recurrent neural networks, we demonstrated that attention can*  
078 *capture task-induced connectivity patterns*; (iv) We applied the NetFormer model to population  
079 activity recorded from mouse visual cortex, and showed that attention can recover experimentally  
080 measured synaptic connectivity, while benchmarking it with standard recurrent models and other  
081 common statistical metrics. Additionally, *we demonstrated that attention can naturally reflect state-*  
082 *dependent modulations in the inferred cell-type level connectivity, even more effectively compared to*  
083 *two other specialized baseline methods.*

## 084 1.1 RELATED WORK

085 **Dynamical models of neuronal activity.** Dynamical models have been a powerful tool for high-  
086 dimensional neural data analysis (Vyas et al., 2020). Generalized linear models (GLMs), known for  
087 both interpretability and desirable convexity properties (Paninski et al., 2007), have been widely used  
088 to model neuronal population activity as well as inter-neuronal interactions (Pillow et al., 2008; Das  
089 & Fiete, 2020). Nevertheless, unless stacked with an explicit state switching mechanism (Escola et al.,  
090 2011), in GLMs the weight matrix describing interactions among neurons is typically stationary across  
091 time (Li et al., 2024). Recurrent neural networks (RNNs) have been a popular alternative (Barak,  
092 2017; Perich et al., 2020); while the connectivity in (trained) RNNs is typically given by a static  
093 connectivity matrix “ $W$ ”, variants including long short-term memory networks (LSTMs) (Hochreiter  
094 & Schmidhuber, 1996) and gated recurrent neural networks (GRUs) (Cho et al., 2014), do include  
095 nonstationarities at the level of individual neural units. While this can enhance the model’s expressivity  
096 and performance in predictive tasks (Salinas et al., 2020; Lai et al., 2018), it also introduces challenges  
097 for interpretability (Tank et al., 2021). Recently, transformer models (Vaswani et al., 2017) have been  
098 observed to outperform RNNs in various time series forecasting tasks (Zhou et al., 2021; Wu et al.,  
099 2021), but their deep layered structures and nonlinear attention mechanisms also raise challenges in  
100 interpretation with respect to underlying connectivity structures in the original data (Jain & Wallace,  
101 2019; Abnar & Zuidema, 2020), as discussed more below. A closely related approach to the present  
102 work is the switching linear dynamical systems (Fox et al., 2008; Linderman et al., 2017a). These  
103 models have nonstationary connectivity matrices which switch among a number of discrete values  
104 according to a Markov process. Nevertheless, in vivo experiments have revealed that cortical activity  
105 is more likely to go through a continuum of states instead of discrete switching (Harris & Thiele,  
2011). This motivates us to propose a model capable of capturing continuous changes in connectivity.

106 **Interpretability of the attention mechanism.** Attention weights and positional embeddings provide  
107 opportunities to understand the inner working of the transformer models. However, the interpretability  
of these components is still a subject of debate. Findings supporting a certain level of interpretability,

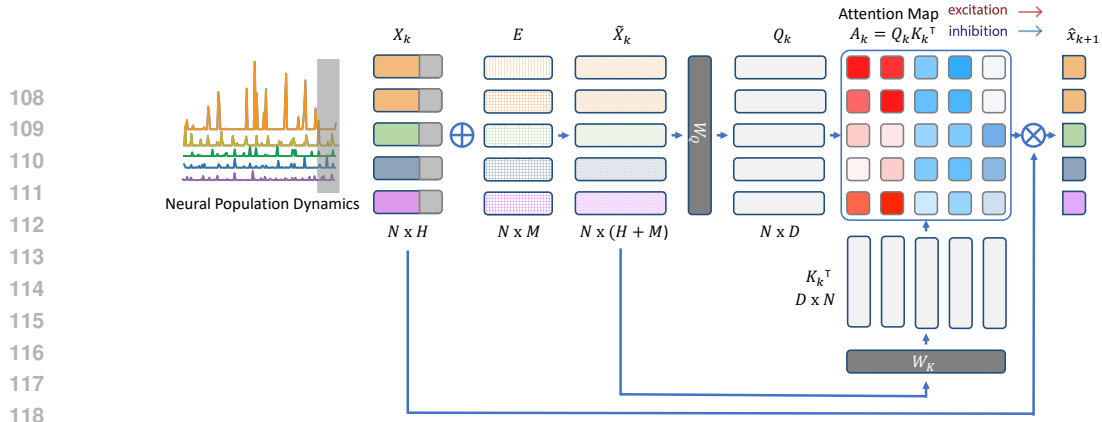


**Figure 1: Overview of NetFormer.** NetFormer learns to predict neural dynamics and infer dynamical connectivity through a linearized attention mechanism. The model takes in activities  $\mathbf{X}_k$  of  $N$  neurons across  $H$  history timesteps, and predicts their activity  $\mathbf{x}_{k+1}$  at timestep  $k + 1$ . Queries  $\mathbf{Q}_k$  and keys  $\mathbf{K}_k$  are linearly mapped from  $\tilde{\mathbf{X}}_k$  ( $\mathbf{X}_k$  concatenated with positional embedding  $\mathbf{E}$ ), using  $\mathbf{W}_Q$  and  $\mathbf{W}_K$ . The time-dependent linearized attention matrix  $\mathbf{A}_k$  is computed as  $\mathbf{Q}_k \mathbf{K}_k^\top$ , which learns the neuron-level dynamical connectivity. Red and blue colors in the attention map indicate excitatory and inhibitory interactions, respectively.

such as correlation to linguistic features, are common in the literature, with specialized metrics developed to quantify their interpretability (Clark et al., 2019; Abnar & Zuidema, 2020). However, caution should be taken when equating attention with explanation (Jain & Wallace, 2019), considering the lack of identifiability (Brunner et al., 2019) and the wide variety of underlying architectures and implementations (Wang & Chen, 2020). In this work, we seek to avoid these confounding aspects by focusing on the linearized attention mechanism (Schlag et al., 2021).

**Predicting activity from connectivity.** The reverse direction, predicting activity from connectivity, is an allied approach for studying the complexities relating functional and structural information. A prominent line of study has focused on the worm *C. elegans* as its synaptic connectome was the first available among all species (White et al., 1986). Using this, generative models of activity have been proposed (Mi et al., 2021). Nevertheless, decades of electrophysiological analyses have emphasized the strong additional role of neuromodulators in shaping activity (Randi et al., 2023; Marder, 2012). As a result, the synaptic connectome alone predicts only partial information about recorded population dynamics (Bargmann, 2012; Randi & Leifer, 2020).

## 2 AN INTERPRETABLE MODEL FOR RECOVERING DYNAMIC CONNECTIVITY

We consider an  $N$ -dimensional dynamical system

$$\frac{d}{dt} \mathbf{x}(t) = f(\mathbf{W}(t)\mathbf{x}(t)) \quad (1)$$

where  $\mathbf{x}(t) \in \mathbb{R}^N$ ,  $f: \mathbb{R}^N \rightarrow \mathbb{R}^N$ , and  $\mathbf{W}(t)$  is an  $N \times N$  matrix whose entries may vary across time.  $W_{i,j}(t)$  prescribes how the  $i$ -th variable  $x^{(i)}$  is driven by the  $j$ -th variable  $x^{(j)}$  at time  $t$ .

Let  $\mathbf{x}_k$  be observations of the system at discrete timesteps  $t_k$ . For each  $k$ , we train the NetFormer model (Figure 1) to predict  $\mathbf{x}_{k+1}$  based on  $\mathbf{X}_k = [\mathbf{x}_{k-H+1} \ \cdots \ \mathbf{x}_k] \in \mathbb{R}^{N \times H}$ , the recent  $H$ -step history of the system up to timestep  $k$ . To encode neuronal identities, a learnable positional embedding matrix  $\mathbf{E} \in \mathbb{R}^{N \times M}$  is concatenated to  $\mathbf{X}_k$ , giving  $\tilde{\mathbf{X}}_k = [\mathbf{X}_k \ \mathbf{E}] \in \mathbb{R}^{N \times (H+M)}$ . The queries  $\mathbf{Q}_k$  and keys  $\mathbf{K}_k$  are obtained through linear transformations of  $\tilde{\mathbf{X}}_k$ , and their product gives the linearized attention matrix  $\mathbf{A}_k$ :

$$\mathbf{Q}_k = \tilde{\mathbf{X}}_k \mathbf{W}_Q \in \mathbb{R}^{N \times D}, \quad \mathbf{K}_k = \tilde{\mathbf{X}}_k \mathbf{W}_K \in \mathbb{R}^{N \times D}, \quad \mathbf{A}_k = \mathbf{Q}_k \mathbf{K}_k^\top \in \mathbb{R}^{N \times N}. \quad (2)$$

It follows that entry  $(i, j)$  of  $\mathbf{A}_k$  is computed from the history of  $x^{(i)}$  and  $x^{(j)}$ , and thus describes the relationship between the  $i$ -th and  $j$ -th variables. To predict  $\mathbf{x}_{k+1}$ , we take  $\mathbf{x}_k$  to be the values  $\mathbf{v}_k$  and employ the residual connection (He et al., 2016), obtaining prediction as

$$\hat{\mathbf{x}}_{k+1} = \mathbf{v}_k + \mathbf{A}_k \mathbf{v}_k = \mathbf{x}_k + \mathbf{A}_k \mathbf{x}_k, \quad (3)$$

which is similar to the update rule we would get if Equation 1 were simulated using the classical forward Euler method with step size  $\delta$

$$\mathbf{x}_{k+1} = \mathbf{x}_k + \delta f(\mathbf{W}_k \mathbf{x}_k). \quad (4)$$

Since neuronal connections can be either excitatory or inhibitory, but neither effect can be arbitrarily large, we choose  $f$  to be a sigmoidal function with

$$f(0) = 0, f(\bar{x}) = f(0) + f'(0)\bar{x} + O(\bar{x}^3) \text{ for } \bar{x} \text{ within some interval } (-\epsilon, \epsilon) \text{ around } 0^1$$

Equation 4 can thus be written as

$$\mathbf{x}_{k+1} = \mathbf{x}_k + \delta f(\mathbf{W}_k \mathbf{x}_k) = \mathbf{x}_k + \delta f'(0) \mathbf{W}_k \mathbf{x}_k + \delta O(\mathbf{x}_k^3). \quad (5)$$

Comparing equations 3 and 5, we deduce that the linearized attention matrix  $\mathbf{A}_k$  learned by the NetFormer may capture the true interactions between different variables  $\mathbf{W}_k$  by approximating  $\delta f'(0) \mathbf{W}_k$ , especially when  $\epsilon < 1$  and the first order term plays the most significant role. It is not hard to see that this hypothesis also extends to systems in the form of

$$\frac{d}{dt} \mathbf{x}(t) = -\mathbf{x}(t) + f(\mathbf{W}(t) \mathbf{x}(t)), \quad (6)$$

which includes the decaying effect that is commonly present in neural dynamics (Gerstner & Kistler, 2002) (Appendix A.1). We provide empirical evidence for this hypothesis on both forms of systems in the subsequent sections.

### 3 EXPERIMENTS ON SYNTHETIC DATA

#### 3.1 NONLINEAR AND NONSTATIONARY SYSTEMS SIMULATION

We first considered four simplified simulated systems, with variations in the inclusion of nonlinearity and nonstationarity:

$$\text{(a) } \frac{d\mathbf{x}}{dt} = \mathbf{W}\mathbf{x}, \text{ (b) } \frac{d\mathbf{x}}{dt} = \tanh(\mathbf{W}\mathbf{x}), \text{ (c) } \frac{d\mathbf{x}}{dt} = \mathbf{W}(\mathbf{x})\mathbf{x}, \text{ (d) } \frac{d\mathbf{x}}{dt} = \tanh(\mathbf{W}(\mathbf{x})\mathbf{x}),$$

where  $\mathbf{W}(\mathbf{x}) = \mathbf{W}_0 + \mathbf{x}\boldsymbol{\omega}^\top$ . Simulation details are in Appendix A.2.1. All trained NetFormer models are able to make accurate one-step-ahead predictions ( $R^2 = 1.000$ , Figure 2a-d left). Visually, the average linearized attention matrix across timesteps,  $\bar{\mathbf{A}} = \frac{1}{K} \sum_{k=1}^K \mathbf{A}_k$ , provides a good characterization of the average ground-truth dynamical association matrix across timesteps,  $\bar{\mathbf{W}} = \frac{1}{K} \sum_{k=1}^K \mathbf{W}(\mathbf{x}_k)$  (Figure 2a-d right). As a baseline, we consider  $\mathbf{A}_{\text{OLS}}$  from the linear ordinary least squares regression  $\hat{\mathbf{x}}_{k+1} = \mathbf{A}_{\text{OLS}} \mathbf{x}_k$ . We used the Spearman’s rank correlation coefficient ( $\rho$ ) between the off-diagonal entries of  $\bar{\mathbf{A}}$  or  $\mathbf{A}_{\text{OLS}}$  and  $\bar{\mathbf{W}}$  to quantify how faithfully the learned connectivities reflect the ground-truth.  $\bar{\mathbf{A}}$  achieved comparable performance as  $\mathbf{A}_{\text{OLS}}$  in systems (a) (b), but significantly outperformed  $\mathbf{A}_{\text{OLS}}$  in systems (c) (d), both visually (Figure 2a-d right) and quantitatively (Appendix A.2.2). Moreover, in the nonstationary systems (c) (d), the linearized attention matrix is able to track the majority of changes in  $\mathbf{W}(\mathbf{x})$  across timesteps (Figure 2e-f and Appendix A.2.3). This ability to capture nonstationarity also explains why NetFormer can outperform the linear regression model which only accounts for static connectivity.

#### 3.2 SPIKE-TIMING-DEPENDENT PLASTICITY (STDP) SIMULATION

Next, we tested NetFormer in a more neurobiological realistic setting by considering a leaky integrate-and-fire (LIF) neuron (Gerstner & Kistler, 2002) with spike-timing-dependent plasticity (STDP). STDP is a fundamental and widely studied synaptic modification scheme in neuroscience (Bi & Poo, 1998; Abbott & Nelson, 2000; Gerstner et al., 1996; Song et al., 2000) where the synaptic connection strength between two neurons depends on the relative timing of the spikes they fire. In typical models, when the presynaptic neuron fires before the postsynaptic neuron, their connection strengthens, increasing the postsynaptic response to future spikes. Conversely, presynaptic firing after postsynaptic weakens the connection. The amount of change in synaptic strength depends on the time interval between pre- and postsynaptic spikes. An example relationship is illustrated in Figure 3a.

We simulated a postsynaptic LIF neuron receiving excitatory inputs from 100 presynaptic neurons, following Neuromatch Academy (2023) (see Appendix A.3 for simulation details). Since we only need the spike times of presynaptic neurons, instead of simulating their dynamics, we directly

<sup>1</sup>see Appendix A.2.4 for more discussion on the radius of convergence of this series representation

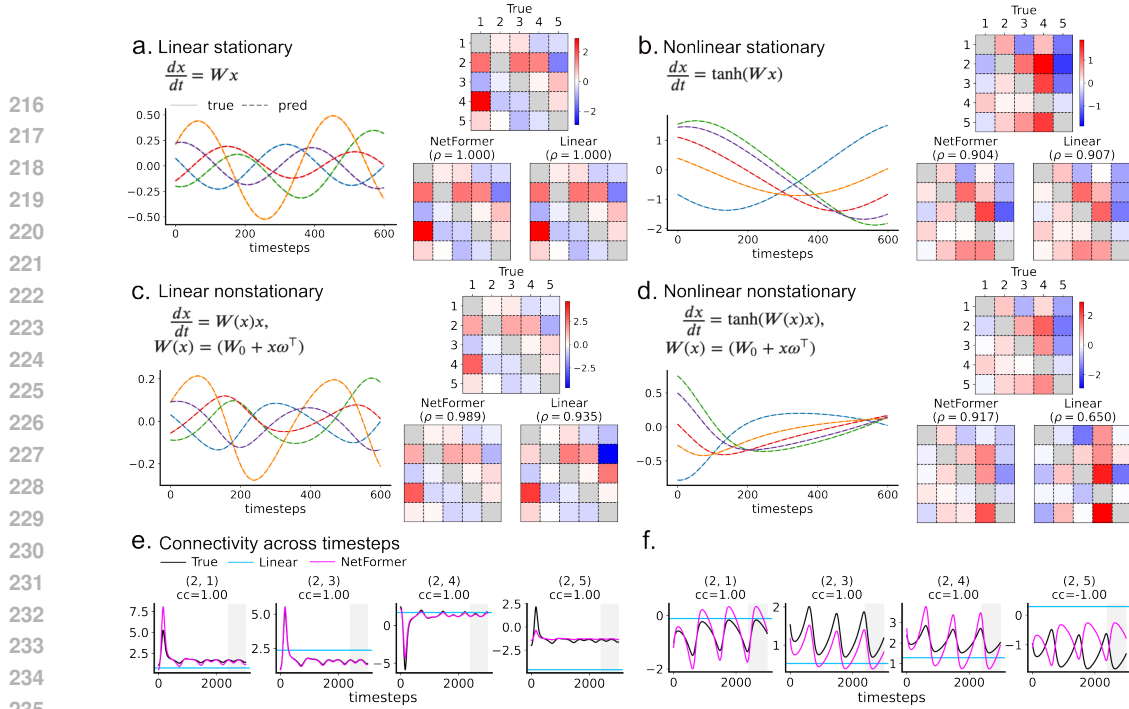


**Figure 2: NetFormer provides accurate dynamics predictions, and recovers ground truth connectivity matrices.** **a-d Left:** Test set predictions of NetFormer. Predicted trajectories were obtained by concatenating all one-step-ahead predictions. Predicted (dashed) trajectories overlap with the true (solid) trajectories. **a-d Right:** True and inferred connectivity from NetFormer’s linearized attention matrix or linear regression weight matrix. For systems **c**, **d**, connectivity is averaged across test set timesteps for visualization. For NetFormer, the inferred connectivity shown is the one whose Spearman correlation  $\rho$  is closest to the average  $\rho$  across 10 random seeds. Colorbars: scale of off-diagonal entries. Diagonal entries are masked in grey. Inferred connectivity matrices were rescaled by the reciprocal of simulation stepsize for visualization. **e:** True and inferred temporal evolution of four example connections in the nonstationary system **c**. Timesteps used as test set are shaded in grey. **f:** True and inferred temporal evolution in system **d**.

modeled their spike trains with independent Poisson processes (Figure 3b). When a spike arrives at a certain synapse, the membrane potential of the LIF neuron is increased by an amount proportional to the synaptic strength, and this potential is reset once the firing threshold is reached (see Appendix A.3 for precise equations). The strength, or weight, of each synapse is modulated following STDP (Figure 3a) within some boundaries. The weight evolution of ten example synapses across the simulation timespan is shown in Figure 3c.

We trained NetFormer to predict the next-step membrane potential of the LIF neuron based on its present and past potential and the spikes it received. This relationship is captured by the  $1 \times 101$  linearized attention matrix of NetFormer. After training, NetFormer is able to capture the dynamics well (test set  $\text{MSE}=0.055 \pm 0.008$ ,  $R^2=0.912 \pm 0.013$ , mean  $\pm$  std across 5 random seeds), outperforming the linear regression model (test set  $\text{MSE}=0.138$ ,  $R^2=0.777$ ). Visualization of their predictions (Figure 3d) shows that NetFormer effectively captures the nonlinear reset mechanism, whereas the linear regression model fails.

We further extracted the learned pre-to-postsynaptic neuron relationship from the linearized attention matrix of NetFormer and compared it against the ground-truth synaptic weights. Unlike the toy systems in Section 3.1 (Figure 2e, f), recovering individual synaptic weights at each timestep from the attention scores does not seem viable. This is not surprising, though, given that the weight differences between synapses are much smaller compared to the membrane potential, that a synapse is only involved in dynamics prediction when it has a spike, and the strong nonlinearity in the membrane spiking dynamics. Nevertheless, we found that for most synapses, the long-term trends in the corresponding attention scores across timesteps are consistent with the true trends in synaptic weights driven by STDP (Figure 3e, f). Across the 100 synapses, the median of the correlation coefficients between smoothed synaptic weight evolution trajectories inferred from attention and the true weight trajectories is  $0.608 \pm 0.028$  (mean  $\pm$  std across 5 seeds). This demonstrates that the simple structure of NetFormer is capable of capturing nonstationary connectivity in spiking neuronal networks with dynamic synapses.

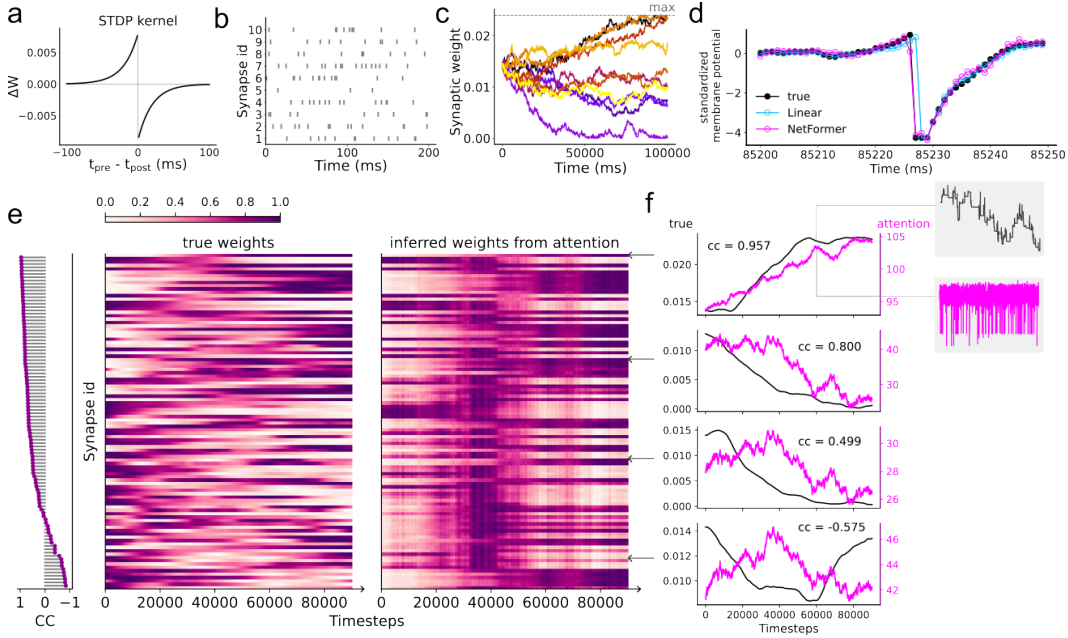


**Figure 3: NetFormer captures the effect of spike-timing-dependent plasticity (STDP).** **a.** STDP temporal kernel used in the simulation. Change in the synaptic weight ( $\Delta W$ ) is a function of the delay between pre- and post-synaptic neuron spikes ( $t_{pre} - t_{post}$ ). **b.** Raster plot of spikes received by the LIF neuron at the first 10 synapses during the first 200 timesteps. **c.** Evolution of the first 10 synapses’ weights across the simulated timespan. Each color represents a synapse. **d.** True and predicted membrane potential across 100 timesteps in the test set. Membrane potential was z-scored before all model fitting. Predicted traces were constructed by concatenating one-step-ahead predictions. **e.** True and inferred synaptic evolution across simulation time span, after smoothing. Both true and inferred evolution trajectories were smoothed with a sliding window. Each row represents a synapse, and the rows were sorted by the correlation between the smoothed true and inferred trajectories. The correlation coefficients corresponding to each row are shown on the left. For visualization, each row was rescaled to  $[0, 1]$  through min-max normalization. **f.** Weight evolution trajectories of four example synapses, which correspond to the 1st, 31st, 61st, and 91st rows from **e.**, as indicated by arrows. The trajectories were smoothed but not min-max normalized. Insets: Raw, unsmoothed trajectories in a sliding window.

### 3.3 TASK-DRIVEN POPULATION ACTIVITY SIMULATION

We further examined whether NetFormer can identify task-driven connectivity patterns in neural populations. As single neuron level connectivity in task-performing laboratory animals are hard to measure, we resorted to task-trained recurrent neural network (RNN) models. The RNN models are trained to perform tasks which mirror the ones laboratory animals are trained to perform, and the activity of their recurrent hidden units has been widely adopted in studies of task-driven neural representation and computation (Mante et al., 2013; Sussillo et al., 2015; Yang et al., 2019; Duncker et al., 2020). Here we considered three representative tasks from the NeuroGym toolkit (Molano-Mazon et al., 2022): **a.** Perceptual Decision Making (Britten et al., 1992), **b.** Go-NoGo (Zhang et al., 2019), and **c.** Delay Comparison (Barak et al., 2010). For each task, we trained a RNN model with hidden dynamics

$$\mathbf{h}_k = \tanh(\mathbf{W}_{stim} \mathbf{s}_k + \mathbf{b}_{stim} + \mathbf{W}_{rec} \mathbf{h}_{k-1} + \mathbf{b}_{rec}). \quad (7)$$

Here  $\mathbf{h}_k \in \mathbb{R}^N$  denotes the activity of hidden units, while  $\mathbf{s}_k \in \mathbb{R}^S$  represents the stimulus input at timestep  $k$ .  $\mathbf{W}_{rec} \in \mathbb{R}^{N \times N}$  specifies how current activity is shaped by past activity, and  $\mathbf{W}_{stim} \in \mathbb{R}^{N \times S}$  captures the effect of the present stimulus input.  $\mathbf{b}_{rec} \in \mathbb{R}^N$ ,  $\mathbf{b}_{stim} \in \mathbb{R}^N$  correspond to baseline activity and background input. We used RNN models with 4, 8, and 12 hidden units for tasks **a**, **b**, **c**, respectively. Training details are provided in Appendix A.4.1. For each task, we applied the trained RNN model to perform 1000 trials, and recorded its hidden units activity across timesteps on every trial. Then we trained NetFormer to predict the next-step hidden units activity  $\mathbf{h}_{k+1}$  based on the present and past hidden activity ( $\mathbf{h}_{k-H}, \dots, \mathbf{h}_k$ ) and stimulus inputs ( $\mathbf{s}_{k+1-H}, \dots, \mathbf{s}_{k+1}$ ) on 800 of those trials, and held out the remaining 200 trials for evaluation. Compared to the linear regression model, NetFormer attains higher accuracy in both dynamics prediction and connectivity recovery (Figure 4 and Appendix A.4.2).

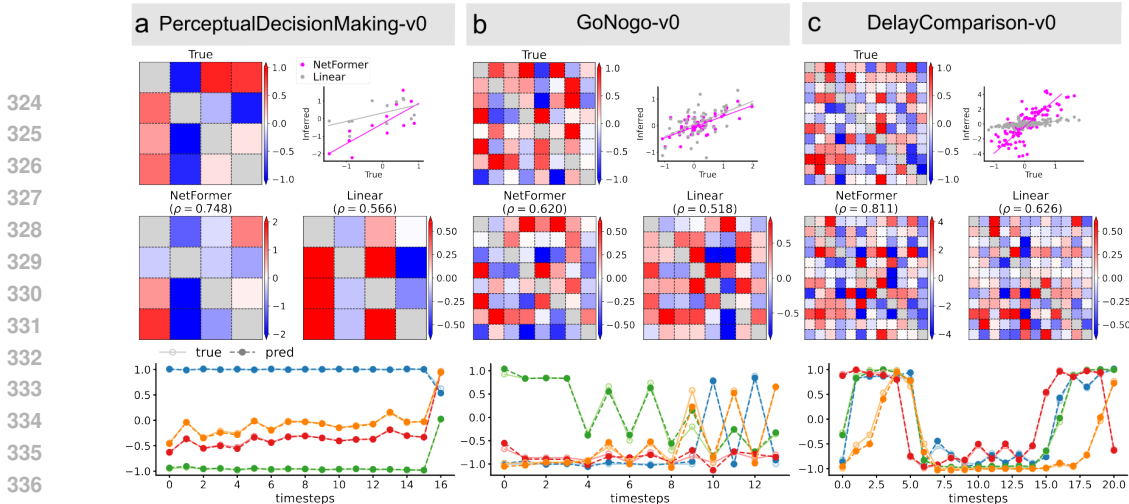


**Figure 4: NetFormer captures task-induced connectivity patterns.** **a.** **Top:** True connectivity matrix from RNN trained to perform the Perceptual Decision Making task, followed by inferred connectivity from NetFormer’s linearized attention matrix or linear regression weight matrix. For NetFormer, the inferred connectivity shown is the one whose Spearman correlation  $\rho$  is closest to the average  $\rho$  across 5 random seeds. Colorbars: scale of off-diagonal entries. Diagonal entries are masked in grey. **Inset:** Scatter plot of off-diagonal entries in the visualized inferred versus true connectivity matrix. **Bottom:** True (solid line, open circles) and NetFormer-predicted (dashed line, filled circles) activity for 4 example hidden units on a held-out trial. Predicted traces were obtained by concatenating one-step-ahead predictions. Hidden units are distinguished by colors. **b-c.** Same as **a**, for RNNs trained to perform the Go-Nogo task and Delay Comparison task, respectively.

#### 4 CONNECTIVITY-CONSTRAINED SIMULATION AND NEURAL DATA

Neurons form synapses based, in part, on factors controlled by their genetic and morphological *cell types*. The transmission of information through these synapses is influenced by activity history and behavioral states. To test its ability to handle these and allied complexities, we applied the NetFormer to a recent multi-modal dataset from (Bugeon et al., 2022), containing both simultaneously recorded neuronal activity and cell type information in the mouse primary visual cortex. After training the NetFormer to predict the neural activity, we used the time-averaged attention matrix as an inferred connectivity strength between neurons. We compared this inferred connectivity against an independent experimental measurement that serves as a cell-type level ground truth. This is the cell-type averaged postsynaptic potential (PSP) measured directly using paired patch-clamp experiments (Campagnola et al., 2022), in which the postsynaptic voltage responses of individual “downstream” neurons are recorded in response to spikes elicited in specific “paired” neurons. As an additional test, we observed that the inferred dynamical connectivity is more similar within the same behavioral state and more distinct between different states. Furthermore, following the measured cell-type level connectivity, we developed a connectivity-constrained simulation to produce neural dynamics with a fully specified ground truth connectivity. On this simulated dataset, we assessed the NetFormer’s ability to infer both individual-neuron level and cell-type level connectivities. More details are in Appendix A.5.

##### 4.1 DATASETS

**Multi-modal in-vivo neural recording.** The publicly available dataset (Bugeon et al., 2022) includes spontaneous population activity recorded from the mouse primary visual cortex (V1) via two-photon calcium imaging. We trained NetFormer models on data from one subject (SB025), which includes recordings of 2481 neurons. The dataset also provides single-cell spatial transcriptomics data, enabling identification of excitatory (EC) and three inhibitory neuron subclasses (Pvalb, Sst, Vip).

**Connectivity-constrained simulation.** We generated activity of a synthetic neuron population with 200 neurons whose cell-type level connectivity is constrained by the aforementioned patch clamp experiments (Campagnola et al., 2022). Specifically, we simulated the leaky-integration system

$$\frac{d}{dt} \mathbf{x}(t) = -\mathbf{x}(t) + \tanh(\mathbf{W} \mathbf{x}(t) + \mathbf{b}) + \epsilon \tag{8}$$

using the forward Euler scheme with a step size  $\delta = 1$ , obtaining in discrete timesteps

$$\mathbf{x}_{k+1} = \tanh(\mathbf{W}\mathbf{x}_k + \mathbf{b}) + \epsilon. \quad (9)$$

Here  $\epsilon$  stands for Gaussian observation noise,  $\mathbf{b}$  represents the baseline activity, and  $\mathbf{W}$  denotes the neuronal connectivity. In our simulation, 76% of neurons are excitatory, with the remaining 24% being inhibitory. The inhibitory neurons are further evenly subdivided into three cell types (Pvalb, Sst, and Vip). We used cell-type specific means and variances of PSPs measured in the patch clamp experiments to define Gaussian distributions of connection strengths between each pair of cell types, and sampled the connection strength between individual cells accordingly. We also provide an additional simulation in Appendix A.7, where the tanh is replaced with a sigmoid nonlinearity.

## 4.2 BASELINES AND EVALUATION METRICS

We benchmarked NetFormer against multiple baselines: (i) a linear recurrent model (referred to as “linear regression”), where  $\mathbf{x}_{k+1} = \mathbf{W}\mathbf{x}_k + \mathbf{b}$ ; two variants of nonlinear recurrent neural networks (referred to as “RNNs”): (ii)  $\mathbf{x}_{k+1} = \tanh(\mathbf{W}\mathbf{x}_k + \mathbf{b})$ , which matches the connectivity-constrained simulation and serves as an “oracle” type model giving a corresponding upper bound on performance, (iii)  $\mathbf{x}_{k+1} = \exp(\mathbf{W}\mathbf{x}_k + \mathbf{b})$ , of the form of commonly used generalized linear models (GLMs) in neuroscience (Pillow et al., 2008), with a nonlinearity mismatched to that of the simulation itself. We also considered standard statistical metrics, including cross-correlation, covariance, mutual information, and transfer entropy (with details in Appendix A.6). We evaluated activity prediction using mean squared error (MSE), coefficient of determination ( $R^2$ ), and the Pearson correlation coefficient. We assessed the correlation between inferred and true connectivity using Pearson and Spearman correlation coefficients, both at the  $N \times N$  neuron level ( $N$ : number of recorded neurons) and the  $K \times K$  cell type-level ( $K = 4$  includes one excitatory and three inhibitory types: Pvalb, Sst, Vip). More details are provided in Appendix A.10.2.

## 4.3 TIME-AVERAGED CONNECTIVITY INFERENCE

**NetFormer outperforms baselines in inferring time-averaged connectivity.** As shown in Table 1 and Figure 5a, on both simulated and real neuronal activity data, NetFormer outperforms other baseline models in predicting activity and inferring connectivity in the majority of the evaluations. We hypothesize that NetFormer’s advantage relative to other baseline methods mainly stem from two key aspects. The first is that the underlying connectivity in the NetFormer model is nonstationary rather than static, as assumed by the other baseline models and methods. The second is the absence of a need to specify an activation nonlinearity. Notable, in the connectivity-constrained simulation, NetFormer achieves comparable performance to the “oracle” model (RNN with tanh nonlinearity). By contrast, the RNN with an exponential nonlinearity, misspecified with respect to the simulation, performed significantly worse. This contrast illustrates a strength of the NetFormer model: NetFormer does not involve specification of an activation function, avoiding the fragility that this can entail. We further tested NetFormer’s robustness to spurious correlations following Das & Fiete (2020) (see details in Appendix A.9). NetFormer shows some resilience to spurious correlations, but would also struggle when the recurrent weights are too strong or too weak, similar to other methods studied in Das & Fiete (2020), including the GLM (Pillow et al., 2008), logistic regression (Lee et al., 2006), and the Ising model (Roudi et al., 2009).

**Excitation cell type can be decoded from learned positional embeddings.** Following Mi et al. (2024), we also observe that the learned positional embeddings  $\mathbf{E}$  in the NetFormer model can be used to decode an aspect of cell class information. Specifically, using learned embeddings of neurons in the training set, we trained a binary classifier via logistic regression to classify neurons as excitatory or inhibitory, a coarser grouping which subsumes the genetic/morphological categories considered above. When applied to classify held-out neurons on the test set, the trained classifier attains 100% top-1 accuracy in simulation data, 66.67% top-1 accuracy and AUROC score of 0.700 in real data (see confusion matrices in Figure 5b). This shows that the learned positional embeddings are linearly separable according to this aspect of neurons’ cell type identity.

**NetFormer demonstrates robustness against partial observation.** For most biological neuronal circuits, each recording can only access the activity of a subset of all neurons. To evaluate its robustness against such partial observation, we fitted NetFormer to a randomly selected subset of neurons in the simulated dataset. In Figure 5c, we show that the performance in recovering the



		NetFormer	linear regression	RNN w/ tanh	RNN w/ exp	cross correlation	covariance	mutual information	transfer entropy	
simulation	connectivity $N \times N$	Pearson	$0.869 \pm 0.002$	$0.817 \pm 0.002$	$0.905 \pm 0.000^*$	$0.581 \pm 0.011$	0.823	-0.029	0.539	0.600
		Spearman	$0.532 \pm 0.001$	$0.507 \pm 0.001$	$0.546 \pm 0.000^*$	$0.393 \pm 0.009$	0.519	-0.015	0.262	0.339
	connectivity $K \times K$	Pearson	$0.879 \pm 0.001$	$0.885 \pm 0.001$	$0.908 \pm 0.000^*$	$0.887 \pm 0.008$	<b>0.888</b>	-0.438	0.371	0.419
		Spearman	$0.860 \pm 0.002$	$0.852 \pm 0.005$	$0.866 \pm 0.002^*$	$0.822 \pm 0.025$	0.732	-0.334	0.018	0.353
in-vivo recording	connectivity $K \times K$	Pearson	$0.777 \pm 0.047$	$-0.395 \pm 0.020$	$-0.395 \pm 0.036$	$-0.407 \pm 0.006$	-0.017	-0.162	-0.176	0.075
		Spearman	$0.847 \pm 0.063$	$-0.409 \pm 0.051$	$-0.343 \pm 0.105$	$-0.191 \pm 0.300$	-0.080	-0.190	-0.061	0.233
	activity prediction	MSE	$0.404 \pm 0.004$	$0.443 \pm 0.001$	$0.560 \pm 0.001$	$0.476 \pm 0.003$	-	-	-	-
		Pearson	$0.740 \pm 0.003$	$0.720 \pm 0.001$	$0.639 \pm 0.000$	$0.699 \pm 0.002$	-	-	-	-
		$R^2$	$0.548 \pm 0.004$	$0.515 \pm 0.001$	$0.386 \pm 0.001$	$0.478 \pm 0.004$	-	-	-	-

**Table 1: NetFormer outperforms classical baselines methods in dynamics prediction and connectivity inference.** Results from both connectivity-constrained simulation and neural recording. An asterisk (\*) indicates that the RNN with tanh activation serves as the oracle model (upper bound for performance on the simulation data). Results from mutual information and transfer entropy are compared against the absolute values of ground truth connectivity. Simulation data has ground truth for both neuron-level ( $N \times N$ ) and cell type-level ( $K \times K$ ) connectivity. Patch-clamp results serve as the ground truth for real neural data cell-type level connectivity. Connectivity inference is assessed with Spearman’s and Pearson’s correlations. Next-step activity prediction is evaluated with MSE, Pearson’s coefficient, and  $R^2$  on the test set.

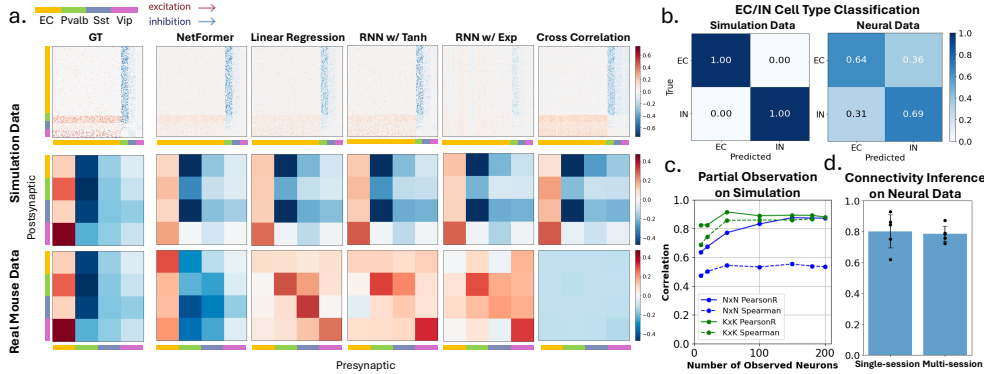


**Figure 5: a.** Visualization of true and inferred connectivities at both neuron level and cell-type level in simulation data and neural data. NetFormer is benchmarked with linear regression, RNNs, and standard statistical metrics. A positive linear transformation has been applied to standardize all matrices to the same range for better visualization. **b.** Confusion matrices of excitatory (EC) and inhibitory (IN) cell type classification on both connectivity-constrained simulation and neural data. **c.** Experiment on different levels of partial observability in the connectivity-constrained simulation. Connectivity inference is evaluated at both neuron level and cell-type level. **d.** Connectivity inference in real neural data with NetFormer models trained on a single session and multiple sessions from the same subject. Errorbars: Spearman correlations across 5 random seeds.

neuron-level connectivity does not decrease significantly even with only half of the neurons observed. Cell-type level connectivity inference is more robust against such partial observations, highlighting the potential of NetFormer to effectively derive cell-type level connectivity from real neural data.

**NetFormer can fit neural recordings across sessions.** RNN-type models, designed to recover connectivity at the level of individual neurons, cannot easily incorporate data of varying population sizes across experimental sessions. In contrast, NetFormer promotes scalability by allowing parameter sharing ( $W_Q, W_K$ ) across sessions. These parameters are defined in the temporal dimension and thus do not increase with the number of neurons. Figure 5d shows that NetFormer achieves comparable performance for connectivity inference when both fitting a single session and multiple sessions.

#### 4.4 NONSTATIONARY CONNECTIVITY INFERENCE

Building on NetFormer’s ability to capture nonstationary connectivity changes over time in Section 3, we extended this evaluation to real neural data. In this dataset (Bugeon et al., 2022), activity at each timestep is labeled by one of the three behavioral states: running, stationary desynchronized, and stationary synchronized. Figure 6a shows that neurons of different cell types can exhibit different activity patterns across these states, suggesting that neural activity is informative of behavioral states. Thus informed, we explored whether the time-varying attention could capture connectivity changes among these states (see details and visualizations in Appendix A.8). We compared NetFormer with two baseline methods capable of capturing nonstationary connectivity: a low-tensor-rank RNN (LtrRNN) (Pellegrino et al., 2023) and an autoregressive Hidden Markov Model (AR-HMM) (Fox et al., 2008; Linderman et al., 2017b). LtrRNN models trial-varying connectivity using a low rank tensor  $W \in \mathbb{R}^{N \times N \times L}$ , where  $L$  denotes the number of trials. Since our neural data is measured during spontaneous activity without an explicit trial structure, to apply LtrRNN, we constructed “trials” using sliding windows on the data. We note that while NetFormer uses shared parameters

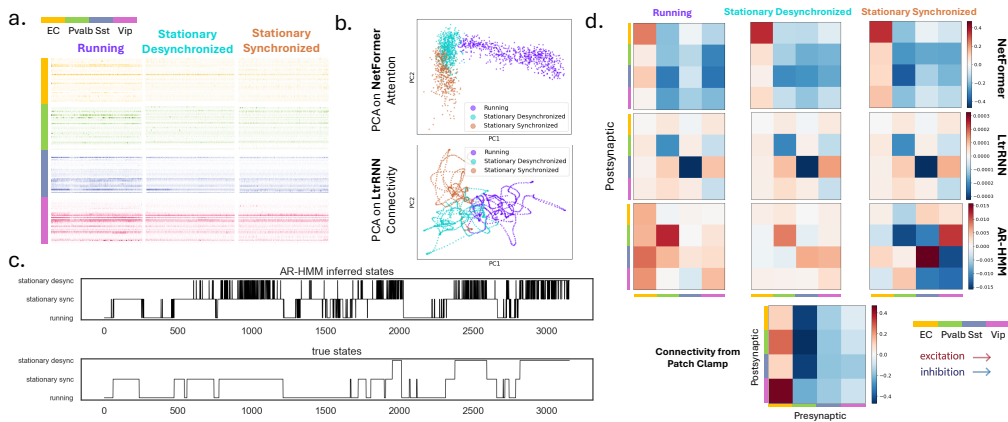


**Figure 6: Connectivity inference across behavioral states.** **a.** Neural activities across cell types in three behavioral states. **b.** Projection of NetFormer attention maps and LtrRNN-inferred connectivity weights onto top two principal components. Each dot represents a different timestep, colored by behavioral states. PCA on NetFormer attention maps shows greater similarity between the two stationary states compared to the running state. **c.** Comparison of AR-HMM inferred states with true behavioral states. **d.** Comparison of inferred state-specific connectivities across NetFormer, LtrRNN, and AR-HMM. NetFormer-inferred connectivities are in better agreement with the patch-clamp result.

across time/trials, LtrRNN trains trial-specific parameters, leading to an explosion in parameters as the number of trials grows. As a second baseline, we considered the AR-HMM, which assumes that there are discrete latent states switching underlying the observed activity, and each state admits unique dynamics through a different connectivity matrix. Due to its discrete state switching mechanism, it is not suitable for capturing continuous connectivity changes, and its state discovery relies heavily on the user-specified number of states.

While NetFormer-inferred cell-type level connectivity is in good agreement with the patch-clamp experimental ground truth, connectivities inferred by LtrRNN and AR-HMM bear little correlation to this ground truth (Figure 6d). A quantitative comparison is provided in Table 6, Appendix A.8. Notably, consistent with prior experimental observations (Fu et al., 2014), attention also witnesses an increase in inhibitory activity from presynaptic Vip neurons and a decrease in inhibition from presynaptic Sst neurons during the running state, as seen by the darker Vip column in the running state compared to the stationary states and the lighter Sst column (Figure 6d, top row). Figure 6b further demonstrates that state information is implicitly captured by NetFormer’s attention maps, showing greater similarity within states and clear distinctions between states. Notably, stationary desynchronized and stationary synchronized states show more similarity to each other than to the running state. Moreover, compared to weights inferred by LtrRNN, PCA on NetFormer-inferred weights yields a cleaner separation between running and two stationary states. When tasked to find three states from the neural data, those inferred by the AR-HMM largely align with the three behavioral states, albeit with higher noise (Figure 6c).

## 5 CONCLUSION AND DISCUSSION

Experience, activity, and adaptation change the effective connectivity of biological neuronal networks via mechanisms including synaptic plasticity and neuromodulation, all playing out across various timescales. This perspective poses connectivity as a dynamical variable that should be tracked, rather than inferred once. Here, we propose the NetFormer as a light-weight model for dynamical connectivity inference. We began with a mathematical analysis that relates nonlinear and nonstationary dynamics to its linearized attention mechanism. We further demonstrated, on representative simulated and in-vivo neural datasets, the strength of our model through comparison against various baselines to predict nonlinear neural dynamics and to capture the underlying dynamical connectivity.

This said, our method has several limitations: (i) Partial observability of neuronal population dynamics has been a major confounding factor for connectivity inference, and our method is no exception. (ii) As our model learns the forward dynamics through a history-dependent linearization of the system in a local temporal neighborhood, its ability to capture nonlinear or nonstationary systems is limited compared to fully nonlinear or layered transformer-type models. Despite these limitations, our work presents a step forward to addressing the long-standing challenge of extracting nonstationary neuronal network structure from complex functional data, and brings new insights into the interpretability of the transformer model and its applicability in modeling nonstationary dynamical systems.

## REFERENCES

- 540  
541  
542 Larry F Abbott and Sacha B Nelson. Synaptic plasticity: taming the beast. *Nature neuroscience*, 3  
543 (11):1178–1183, 2000.
- 544 Samira Abnar and Willem Zuidema. Quantifying attention flow in transformers. *arXiv preprint*  
545 *arXiv:2005.00928*, 2020.
- 546  
547 Kyle Aitken and Stefan Mihalas. Neural population dynamics of computing with synaptic modulations.  
548 *Elife*, 12:e83035, 2023.
- 549  
550 Omri Barak. Recurrent neural networks as versatile tools of neuroscience research. *Current opinion*  
551 *in neurobiology*, 46:1–6, 2017.
- 552  
553 Omri Barak, Misha Tsodyks, and Ranulfo Romo. Neuronal population coding of parametric working  
554 memory. *Journal of Neuroscience*, 30(28):9424–9430, 2010.
- 555  
556 Cornelia I Bargmann. Beyond the connectome: how neuromodulators shape neural circuits. *Bioessays*,  
557 34(6):458–465, 2012.
- 558  
559 Guo-qiang Bi and Mu-ming Poo. Synaptic modifications in cultured hippocampal neurons: depen-  
560 dence on spike timing, synaptic strength, and postsynaptic cell type. *Journal of neuroscience*, 18  
(24):10464–10472, 1998.
- 561  
562 Kenneth H Britten, Michael N Shadlen, William T Newsome, and J Anthony Movshon. The  
563 analysis of visual motion: a comparison of neuronal and psychophysical performance. *Journal of*  
*Neuroscience*, 12(12):4745–4765, 1992.
- 564  
565 Gino Brunner, Yang Liu, Damian Pascual, Oliver Richter, Massimiliano Ciaramita, and Roger  
566 Wattenhofer. On identifiability in transformers. *arXiv preprint arXiv:1908.04211*, 2019.
- 567  
568 Stéphane Bugeon, Joshua Duffield, Mario Dipoppa, Anne Ritoux, Isabelle Prankerd, Dimitris  
569 Nicoloutsopoulos, David Orme, Maxwell Shinn, Han Peng, Hamish Forrest, Aiste Viduolyte,  
570 Charu Bai Reddy, Yoh Isogai, Matteo Carandini, and Kenneth D. Harris. A transcriptomic axis  
571 predicts state modulation of cortical interneurons. *Nature*, 607, 2022. ISSN 1476-4687.
- 572  
573 Luke Campagnola, Stephanie C Seeman, Thomas Chartrand, Lisa Kim, Alex Hoggarth, Clare Gamlin,  
574 Shinya Ito, Jessica Trinh, Pasha Davoudian, Cristina Radaelli, et al. Local connectivity and synaptic  
dynamics in mouse and human neocortex. *Science*, 375(6585):eabj5861, 2022.
- 575  
576 Kyunghyun Cho, Bart Van Merriënboer, Caglar Gulcehre, Dzmitry Bahdanau, Fethi Bougares, Holger  
577 Schwenk, and Yoshua Bengio. Learning phrase representations using rnn encoder-decoder for  
578 statistical machine translation. *arXiv preprint arXiv:1406.1078*, 2014.
- 579  
580 Kevin Clark, Urvashi Khandelwal, Omer Levy, and Christopher D Manning. What does bert look at?  
an analysis of bert’s attention. *arXiv preprint arXiv:1906.04341*, 2019.
- 581  
582 Abhranil Das and Ila R Fiete. Systematic errors in connectivity inferred from activity in strongly  
583 recurrent networks. *Nature Neuroscience*, 23(10):1286–1296, 2020.
- 584  
585 Lea Duncker, Laura Driscoll, Krishna V Shenoy, Maneesh Sahani, and David Sussillo. Organizing  
586 recurrent network dynamics by task-computation to enable continual learning. *Advances in neural*  
*information processing systems*, 33:14387–14397, 2020.
- 587  
588 Sean Escola, Alfredo Fontanini, Don Katz, and Liam Paninski. Hidden markov models for the  
589 stimulus-response relationships of multistate neural systems. *Neural computation*, 23(5):1071–  
590 1132, 2011.
- 591  
592 William Falcon and The PyTorch Lightning team. PyTorch Lightning, March 2019.
- 593  
Emily Fox, Erik Sudderth, Michael Jordan, and Alan Willsky. Nonparametric bayesian learning of  
switching linear dynamical systems. *Advances in neural information processing systems*, 21, 2008.

- 594 Yu Fu, Jason M. Tucciarone, J. Sebastian Espinosa, Nengyin Sheng, Daniel P. Darcy, Roger A. Nicoll,  
595 Z. Josh Huang, and Michael P. Stryker. A cortical circuit for gain control by behavioral state. *Cell*,  
596 156(6):1139–1152, Mar 2014. ISSN 0092-8674. doi: 10.1016/j.cell.2014.01.050.
- 597  
598 Wulfram Gerstner and Werner M Kistler. *Spiking neuron models: Single neurons, populations,*  
599 *plasticity*. Cambridge university press, 2002.
- 600 Wulfram Gerstner, Richard Kempter, J Leo Van Hemmen, and Hermann Wagner. A neuronal learning  
601 rule for sub-millisecond temporal coding. *Nature*, 383(6595):76–78, 1996.
- 602  
603 Kenneth D Harris and Alexander Thiele. Cortical state and attention. *Nature reviews neuroscience*,  
604 12(9):509–523, 2011.
- 605  
606 Kaiming He, Xiangyu Zhang, Shaoqing Ren, and Jian Sun. Deep residual learning for image  
607 recognition. In *Proceedings of the IEEE conference on computer vision and pattern recognition*,  
608 pp. 770–778, 2016.
- 609  
610 Sepp Hochreiter and Jürgen Schmidhuber. Lstm can solve hard long time lag problems. *Advances in*  
*neural information processing systems*, 9, 1996.
- 611  
612 Sarthak Jain and Byron C Wallace. Attention is not explanation. *arXiv preprint arXiv:1902.10186*,  
613 2019.
- 614  
615 Guokun Lai, Wei-Cheng Chang, Yiming Yang, and Hanxiao Liu. Modeling long-and short-term  
616 temporal patterns with deep neural networks. In *The 41st international ACM SIGIR conference on*  
*research & development in information retrieval*, pp. 95–104, 2018.
- 617  
618 Trung Le and Eli Shlizerman. Stndt: Modeling neural population activity with spatiotemporal trans-  
619 formers. In S. Koyejo, S. Mohamed, A. Agarwal, D. Belgrave, K. Cho, and A. Oh (eds.), *Advances*  
*in Neural Information Processing Systems*, volume 35, pp. 17926–17939. Curran Associates, Inc.,  
620 2022.
- 621  
622 Su-In Lee, Honglak Lee, Pieter Abbeel, and Andrew Y Ng. Efficient  $L_1$  regularized logistic  
623 regression. In *Aaai*, volume 6, pp. 401–408, 2006.
- 624  
625 Chengrui Li, Soon Ho Kim, Chris Rodgers, Hannah Choi, and Anqi Wu. One-hot generalized linear  
626 model for switching brain state discovery. In *The Twelfth International Conference on Learning*  
*Representations*, 2024.
- 627  
628 Scott Linderman, Matthew Johnson, Andrew Miller, Ryan Adams, David Blei, and Liam Paninski.  
629 Bayesian learning and inference in recurrent switching linear dynamical systems. In *Artificial*  
*intelligence and statistics*, pp. 914–922. PMLR, 2017a.
- 630  
631 Scott Linderman, Matthew Johnson, Andrew Miller, Ryan Adams, David Blei, and Liam Paninski.  
632 Bayesian Learning and Inference in Recurrent Switching Linear Dynamical Systems. In Aarti Singh  
633 and Jerry Zhu (eds.), *Proceedings of the 20th International Conference on Artificial Intelligence*  
*and Statistics*, volume 54 of *Proceedings of Machine Learning Research*, pp. 914–922. PMLR,  
634 20–22 Apr 2017b.
- 635  
636 Yuhan Helena Liu, Stephen Smith, Stefan Mihalas, Eric Shea-Brown, and Uygur Sümbül. Cell-  
637 type-specific neuromodulation guides synaptic credit assignment in a spiking neural network.  
638 *Proceedings of the National Academy of Sciences*, 118(51):e2111821118, 2021.
- 639  
640 Sindy Löwe, David Madras, Richard Zemel, and Max Welling. Amortized causal discovery: Learning  
641 to infer causal graphs from time-series data. In *Conference on Causal Learning and Reasoning*,  
642 pp. 509–525. PMLR, 2022.
- 643  
644 Ziyu Lu, Anika Tabassum, Shruti Kulkarni, Lu Mi, J Nathan Kutz, Eric Shea-Brown, and Seung-  
645 Hwan Lim. Attention for causal relationship discovery from biological neural dynamics. *arXiv*  
*preprint arXiv:2311.06928*, 2023.
- 646  
647 Valerio Mante, David Sussillo, Krishna V Shenoy, and William T Newsome. Context-dependent  
computation by recurrent dynamics in prefrontal cortex. *nature*, 503(7474):78–84, 2013.

- 648 Eve Marder. Neuromodulation of neuronal circuits: Back to the future. *Neuron*, 76(1):1–11, 2012.  
649 ISSN 0896-6273. doi: <https://doi.org/10.1016/j.neuron.2012.09.010>.
- 650
- 651 Lu Mi, Richard Xu, Sridhama Prakhya, Albert Lin, Nir Shavit, Aravinthan Samuel, and Srinivas  
652 C Turaga. Connectome-constrained latent variable model of whole-brain neural activity. In  
653 *International Conference on Learning Representations*, 2021.
- 654 Lu Mi, Trung Le, Tianxing He, Eli Shlizerman, and Uygur Sümbül. Learning time-invariant  
655 representations for individual neurons from population dynamics. *Advances in Neural Information  
656 Processing Systems*, 36, 2024.
- 657
- 658 Manuel Molano-Mazon, Joao Barbosa, Jordi Pastor-Ciurana, Marta Fradera, Ru-Yuan Zhang, Jeremy  
659 Forest, Jorge del Pozo Lerida, Li Ji-An, Christopher J Cueva, Jaime de la Rocha, et al. Neurogym:  
660 An open resource for developing and sharing neuroscience tasks. 2022.
- 661 Neuromatch Academy. Biological neuron models tutorial, 2023. Accessed: 2024-09-28.
- 662
- 663 Chethan Pandarinath, Daniel J O’Shea, Jasmine Collins, Rafal Jozefowicz, Sergey D Stavisky,  
664 Jonathan C Kao, Eric M Trautmann, Matthew T Kaufman, Stephen I Ryu, Leigh R Hochberg, et al.  
665 Inferring single-trial neural population dynamics using sequential auto-encoders. *Nature methods*,  
666 15(10):805–815, 2018.
- 667
- 668 Liam Paninski, Jonathan Pillow, and Jeremy Lewi. Statistical models for neural encoding, decoding,  
669 and optimal stimulus design. *Progress in brain research*, 165:493–507, 2007.
- 670
- 671 Adam Paszke, Sam Gross, Soumith Chintala, Gregory Chanan, Edward Yang, Zachary DeVito,  
672 Zeming Lin, Alban Desmaison, Luca Antiga, and Adam Lerer. Automatic differentiation in  
673 pytorch. 2017.
- 674
- 675 Arthur Pellegrino, N Alex Cayco Gajic, and Angus Chadwick. Low tensor rank learning of neural  
676 dynamics. *Advances in Neural Information Processing Systems*, 36:11674–11702, 2023.
- 677
- 678 Matthew G Perich, Charlotte Arlt, Sofia Soares, Megan E Young, Clayton P Mosher, Juri Minxha,  
679 Eugene Carter, Ueli Rutishauser, Peter H Rudebeck, Christopher D Harvey, et al. Inferring brain-  
680 wide interactions using data-constrained recurrent neural network models. *BioRxiv*, pp. 2020–12,  
681 2020.
- 682
- 683 Jonathan W Pillow, Jonathon Shlens, Liam Paninski, Alexander Sher, Alan M Litke, EJ Chichilnisky,  
684 and Eero P Simoncelli. Spatio-temporal correlations and visual signalling in a complete neuronal  
685 population. *Nature*, 454(7207):995–999, 2008.
- 686
- 687 Francesco Randi and Andrew M Leifer. Measuring and modeling whole-brain neural dynamics in  
688 *caenorhabditis elegans*. *Current opinion in neurobiology*, 65:167–175, 2020.
- 689
- 690 Francesco Randi, Anuj K Sharma, Sophie Dvali, and Andrew M Leifer. Neural signal propagation  
691 atlas of *caenorhabditis elegans*. *Nature*, 623(7986):406–414, 2023.
- 692
- 693 Yasser Roudi, Joanna Tyrcha, and John Hertz. Ising model for neural data: model quality and  
694 approximate methods for extracting functional connectivity. *Physical Review E—Statistical,  
695 Nonlinear, and Soft Matter Physics*, 79(5):051915, 2009.
- 696
- 697 David Salinas, Valentin Flunkert, Jan Gasthaus, and Tim Januschowski. Deepar: Probabilistic  
698 forecasting with autoregressive recurrent networks. *International journal of forecasting*, 36(3):  
699 1181–1191, 2020.
- 700
- 701 Andrea Santuy, Laura Tomás-Roca, José-Rodrigo Rodríguez, Juncal González-Soriano, Fei Zhu,  
Zhen Qiu, Seth GN Grant, Javier DeFelipe, and Angel Merchan-Perez. Estimation of the number of  
synapses in the hippocampus and brain-wide by volume electron microscopy and genetic labeling.  
*Scientific Reports*, 10(1):14014, 2020.
- 702
- 703 Imanol Schlag, Kazuki Irie, and Jürgen Schmidhuber. Linear transformers are secretly fast weight  
704 programmers. In *International Conference on Machine Learning*, pp. 9355–9366. PMLR, 2021.

- 702 Ryan Singh and Christopher L Buckley. Attention as implicit structural inference. *Advances in*  
703 *Neural Information Processing Systems*, 36:24929–24946, 2023.  
704
- 705 Sen Song, Kenneth D Miller, and Larry F Abbott. Competitive hebbian learning through spike-timing-  
706 dependent synaptic plasticity. *Nature neuroscience*, 3(9):919–926, 2000.
- 707 David Sussillo, Mark M Churchland, Matthew T Kaufman, and Krishna V Shenoy. A neural network  
708 that finds a naturalistic solution for the production of muscle activity. *Nature neuroscience*, 18(7):  
709 1025–1033, 2015.
- 710 Alex Tank, Ian Covert, Nicholas Foti, Ali Shojaie, and Emily B Fox. Neural granger causality. *IEEE*  
711 *Transactions on Pattern Analysis and Machine Intelligence*, 44(8):4267–4279, 2021.  
712
- 713 Danil Tyulmankov, Ching Fang, Annapurna Vadaparty, and Guangyu Robert Yang. Biological  
714 learning in key-value memory networks. *Advances in Neural Information Processing Systems*, 34:  
715 22247–22258, 2021.
- 716 Ashish Vaswani, Noam Shazeer, Niki Parmar, Jakob Uszkoreit, Llion Jones, Aidan N Gomez, Łukasz  
717 Kaiser, and Illia Polosukhin. Attention is all you need. *Advances in neural information processing*  
718 *systems*, 30, 2017.  
719
- 720 Saurabh Vyas, Matthew D Golub, David Sussillo, and Krishna V Shenoy. Computation through  
721 neural population dynamics. *Annual review of neuroscience*, 43:249–275, 2020.  
722
- 723 Yu-An Wang and Yun-Nung Chen. What do position embeddings learn? an empirical study of  
724 pre-trained language model positional encoding. *arXiv preprint arXiv:2010.04903*, 2020.
- 725 John G White, Eileen Southgate, J Nichol Thomson, Sydney Brenner, et al. The structure of the  
726 nervous system of the nematode *caenorhabditis elegans*. *Philos Trans R Soc Lond B Biol Sci*, 314  
727 (1165):1–340, 1986.
- 728 Haixu Wu, Jiehui Xu, Jianmin Wang, and Mingsheng Long. Autoformer: Decomposition transformers  
729 with auto-correlation for long-term series forecasting. *Advances in neural information processing*  
730 *systems*, 34:22419–22430, 2021.  
731
- 732 Guangyu Robert Yang, Madhura R Joglekar, H Francis Song, William T Newsome, and Xiao-Jing  
733 Wang. Task representations in neural networks trained to perform many cognitive tasks. *Nature*  
734 *neuroscience*, 22(2):297–306, 2019.
- 735 Joel Ye, Jennifer L Collinger, Leila Wehbe, and Robert Gaunt. Neural data transformer 2: Multi-  
736 context pretraining for neural spiking activity. In *Thirty-seventh Conference on Neural Information*  
737 *Processing Systems*, 2023.  
738
- 739 Xiaoxing Zhang, Wenjun Yan, Wenliang Wang, Hongmei Fan, Ruiqing Hou, Yulei Chen, Zhaoqin  
740 Chen, Chaofan Ge, Shumin Duan, Albert Compte, et al. Active information maintenance in  
741 working memory by a sensory cortex. *Elife*, 8:e43191, 2019.
- 742 Haoyi Zhou, Shanghang Zhang, Jieqi Peng, Shuai Zhang, Jianxin Li, Hui Xiong, and Wancai Zhang.  
743 Informer: Beyond efficient transformer for long sequence time-series forecasting. In *Proceedings*  
744 *of the AAAI conference on artificial intelligence*, volume 35, pp. 11106–11115, 2021.  
745  
746  
747  
748  
749  
750  
751  
752  
753  
754  
755

756 A APPENDIX

757 A.1 JUSTIFICATION FOR LINEARIZED ATTENTION APPLIED TO “LEAKY” SYSTEMS (EQN 6)

758 Using the forward Euler method and step size  $\delta$ , Equation 6 can be simulated as

759 
$$\mathbf{x}_{k+1} = \mathbf{x}_k + \delta \left( -\mathbf{x}_k + f(\mathbf{W}_k \mathbf{x}_k) \right) = \mathbf{x}_k - \delta \mathbf{x}_k + \delta f(\mathbf{W}_k \mathbf{x}_k). \tag{10}$$

760 Following the same sigmoidal assumption on  $f$ , Equation 10 can be written as

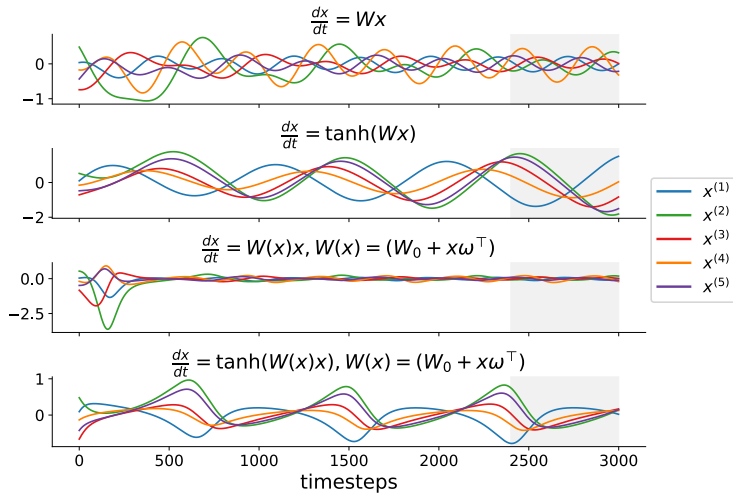
761 
$$\mathbf{x}_{k+1} = \mathbf{x}_k + \delta (f'(0) \mathbf{W}_k - \mathbf{I}) \mathbf{x}_k + \delta O(\mathbf{x}_k^3), \tag{11}$$

762 where  $\mathbf{I}$  is the  $N \times N$  identity matrix. Therefore, the linearized attention matrix  $\mathbf{A}_k$  learned from  
 763 Equation 3 may reflect the true interactions  $\mathbf{W}_k$  by approximating  $\delta (f'(0) \mathbf{W}_k - \mathbf{I})$ , and can capture  
 764 the interactions between different variables (off-diagonal entries of  $\mathbf{W}_k$ ) up to a scaling factor  
 765 ( $\delta f'(0)$ ).

766 A.2 ADDITIONAL DETAILS FOR NONLINEAR AND NONSTATIONARY SYSTEMS SIMULATION  
 767 (SEC 3.1)

768 A.2.1 SIMULATION DETAILS

769 In Figure 2 a, b, ground-truth  $\mathbf{W}$  were generated randomly, with real-part of each eigenvalue clipped  
 770 at 0 to ensure stability of the system.  $\mathbf{W}$  in a, b were also used as  $\mathbf{W}_0$  in c,d, respectively.  $\omega$  in  
 771 c, d were picked randomly while maintaining stability of the system. In a, the system trajectory  
 772 was simulated using the closed-form solution  $\mathbf{x}(t) = e^{\mathbf{W}t} \boldsymbol{\eta}$ , where  $\boldsymbol{\eta}$  is the initial state. In b-d,  
 773 trajectories were simulated using the forward Euler method:  $\mathbf{x}_{k+1} = \mathbf{x}_k + \delta f(\mathbf{W}_k \mathbf{x}_k)$ , where  
 774  $\mathbf{W}_k \equiv \mathbf{W}$  for b, and  $\mathbf{W}_k = \mathbf{W}_0 + \mathbf{x}_k \boldsymbol{\omega}^\top$  for c, d. All simulations consist of 3000 timesteps  
 775 with stepsize  $\delta = 0.01$ , with the first 80% used as training set, and last 20% as test set. For c, d,  
 776 ground-truth connectivity matrices were computed as the time-averaged connectivity across test set  
 777 timesteps  $\bar{\mathbf{W}} = \sum_{k=2400}^{3000} \mathbf{W}_k$ . Simulated trajectories are visualized in Figure 7. In all settings, the  
 778 NetFormer model was trained to minimize the mean squared error (MSE) on the training set for  
 779 1100 epochs using the Adam optimizer in Pytorch, with  $H = 1, M = 5, D = 5$ , batch size = 80,  
 780 initial learning rate = 0.01. In b, d, learning rate was decayed by a factor of 0.9 every 100 epochs. In  
 781 c, learning rate was decayed by a factor of 0.8 every 100 epochs.

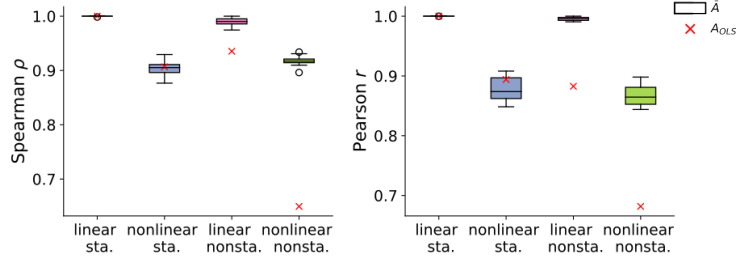


782 **Figure 7:** Simulated trajectories of toy models in Figure 2. Shaded regions represent timesteps used  
 783 as test set.

784 A.2.2 QUANTITIVE COMPARSION WITH LINEAR REGRESSOIN MODEL

785 For each toy system in section 3.1, we trained 10 NetFormer models with different random seeds  
 786 (initializations), and computed the Spearman’s rank correlation coefficient ( $\rho$ ) and the Pearson

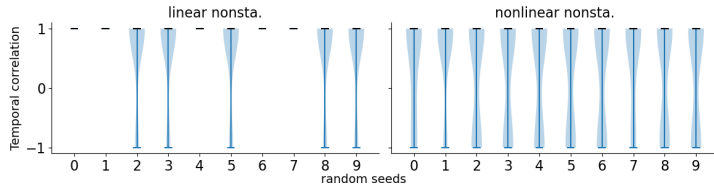
810 correlation coefficient ( $r$ ) between the off-diagonal entries of  $\bar{\mathbf{A}}$  and  $\bar{\mathbf{W}}$  for each trained model.  
 811 In terms of  $\rho$ ,  $\bar{\mathbf{A}}$  achieved comparable performance as  $\mathbf{A}_{\text{OLS}}$  in systems **a**, **b** ( $p > 0.3$ , two-sided  
 812 one sample t test), but significantly outperformed  $\mathbf{A}_{\text{OLS}}$  in systems **c**, **d** ( $p < 10^{-8}$ ) (Figure 8 left).  
 813 Similar observations can be made with  $r$  (Figure 8 right). For each system, the linearized attention  
 814 matrix visualized in Figure 2 is the one whose  $\rho$  is the closest to the average  $\rho$  across 10 random seeds.  
 815



825 **Figure 8:** Comparison between  $\mathbf{A}_{\text{OLS}}$  (red cross) and  $\bar{\mathbf{A}}$  from NetFormer models with 10 different  
 826 random initializations (boxplots).  
 827

828  
 829 **A.2.3 NONSTATIONARITY CONNECTIVITY TRACKING**

830 On toy systems with nonstationary connectivity (Figure 2c, d), we evaluated how well linearized  
 831 attention matrices across timesteps can track changes in the connectivity. For each pair  $(i, j)$ ,  $i, j =$   
 832  $1, \dots, 5, i \neq j$ , we collected  $\mathbf{A}_{ij}$  and  $\mathbf{W}_{ij}$  across all test timesteps, resulting in two time-varying  
 833 series  $\mathbf{A}_{ij}(t)$  and  $\mathbf{W}_{ij}(t)$ , and computed the Pearson correlation coefficient between them. Results  
 834 for 10 trained NetFormer models with different random seeds are shown in Figure 9. Distributions  
 835 of the temporal correlation coefficients for all off-diagonal pairs  $(i, j)$  are shown as violin plots, where  
 836 each violin corresponds to model trained with one random seed. The median of each distribution is  
 837 marked with a black line. All medians are greater than 0.999.  
 838



845 **Figure 9:** Distribution of test set temporal correlation between the linearized attention matrix and the  
 846 true nonstationary connectivity. Each column shows result from NetFormer model with a different  
 847 random seed. Median of each distribution is marked in black. All medians are greater than 0.999.  
 848

849  
 850 **A.2.4 FURTHER DISCUSSION ON NONLINEAR DYNAMICAL SYSTEMS**

851 In Section 2, we showed that when  $f$  is sigmoidal,  $\mathbf{A}$  can reflect  $\mathbf{W}$  through Taylor series approx-  
 852 imation of  $f(\mathbf{W}\mathbf{x}_k)$ . Take  $f = \tanh$  as an example. Let  $\mathbf{w}_i$  denote the  $i$ -th row of  $\mathbf{W}$ . When  
 853  $|\mathbf{w}_i^\top \mathbf{x}_k| < \frac{\pi}{2} \forall i = 1, \dots, N$ ,

$$854 \quad \tanh(\mathbf{W}\mathbf{x}_k) = \tanh(0) + \tanh'(0)\mathbf{W}\mathbf{x}_k + O(\mathbf{x}_k^3).$$

855 As  $\tanh(0) = 0$ , the forward Euler method is

$$856 \quad \mathbf{x}_{k+1} = \mathbf{x}_k + \delta \tanh(\mathbf{W}\mathbf{x}_k) = \mathbf{x}_k + \delta \tanh'(0)\mathbf{W}\mathbf{x}_k + \delta O(\mathbf{x}_k^3).$$

857 This analysis also applies to other sigmoidal functions  $f$ , such as  $\arctan$ , with

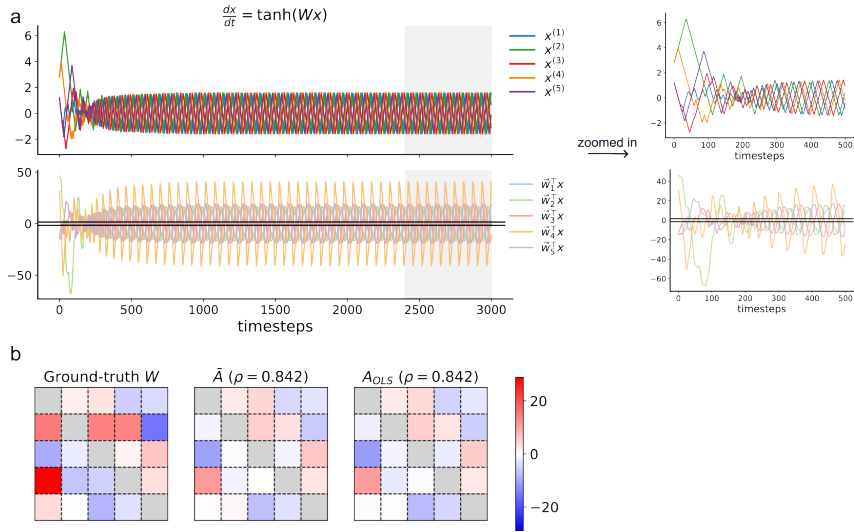
$$858 \quad f(0) = 0, f(\bar{x}) = f'(0)\bar{x} + O(\bar{x}^3) \text{ for } \bar{x} \text{ within some interval around } 0.$$

859 Therefore, we hypothesize that  $\mathbf{A}$  can capture  $\mathbf{W}$  through learning  $\delta f'(0)\mathbf{W}$  for sigmoidal  $f$ . It is  
 860 also clear that learning  $\mathbf{W}$  becomes more challenging when  $\mathbf{w}_i^\top \mathbf{x}$  does not always stay within the  
 861 radius of convergence of the Maclaurin series. Nonetheless, we note that if some  $\mathbf{w}_i^\top \mathbf{x}$  is constantly  
 862  
 863



864 outside the convergence region,  $f(\mathbf{w}_i^\top \mathbf{x})$  will be constantly positive or negative, and the system will  
 865 either blow up or decay to zero. Therefore, for the systems of interest here, which are those with  
 866 interesting persistent dynamics, from time to time  $\mathbf{w}_i^\top \mathbf{x}$  must fall within the convergence region  
 867 where the Maclaurin series representation is valid. That being said, while  $\mathbf{A}$  may still be able to  
 868 capture some aspect of  $\mathbf{W}$ , it could become less accurate, and may require more observations of the  
 869 system to gather sufficient timesteps within the convergence region.

870 In the example nonlinear dynamical system shown in Figure 2b,  $\mathbf{w}_i^\top \mathbf{x}_k$  stays within the radius of  
 871 convergence of  $\tanh$  for all  $i$  and  $k$ , which makes the Maclaurin series approximation valid for all  
 872 timesteps. In Figure 10, we provide another toy model example showing that the attention from  
 873 NetFormer still bears considerable similarity to the ground-truth  $\mathbf{W}$  even when  $\mathbf{w}_i^\top \mathbf{x}_k$  falls out of  
 874 the convergence region for some  $i$  and  $k$ .



887 **Figure 10:** Demonstration of NetFormer on a nonlinear system  $\frac{dx}{dt} = \tanh(\mathbf{W}\mathbf{x})$  where  $\mathbf{w}_i^\top \mathbf{x}$   
 888 does not always stay within the convergence region of the Maclaurin series of  $\tanh$ . **a. Top row:**  
 889 Trajectories of the simulated system. Simulation was done using the forward Euler method with  
 890 stepsize  $\delta = 0.1$ . Shaded regions represent timesteps used as test set. **Bottom row:** Visualization  
 891 of  $\mathbf{w}_i^\top \mathbf{x}$  across simulated timesteps. Boundaries of the convergence region,  $\pm \frac{\pi}{2}$ , were marked with  
 892 black horizontal lines. The right column provides a zoomed-in view of the first 500 simulation  
 893 timesteps. **b. Left to right** Ground-truth  $\mathbf{W}$ , average linearized attention matrix across test timesteps  
 894 from NetFormer ( $\bar{\mathbf{A}}$ ),  $\mathbf{A}_{OLS}$  fitted through least-squares regression. Colorbars indicate the scale of  
 895 the off-diagonal entries, and the diagonal entries are masked in grey.  $\bar{\mathbf{A}}$ ,  $\mathbf{A}_{OLS}$  were rescaled for  
 896 visualization. Spearman’s rank correlation coefficients ( $\rho$ ) were computed between the off-diagonal  
 897 entries of  $\bar{\mathbf{A}}$  or  $\mathbf{A}_{OLS}$  and  $\mathbf{W}$ . We trained 10 NetFormer models with different random initializations  
 898 ( $\rho = 0.841 \pm 0.02$ , mean  $\pm$  std), and  $\bar{\mathbf{A}}$  shown is the one whose  $\rho$  is the closest to the average  $\rho$  across  
 899 10 random initializations. NetFormer models achieved similar performance as  $\mathbf{A}_{OLS}$  ( $p = 0.9$ , two-  
 900 sided one sample t test). All NetFormer models were trained to minimize the mean squared error on  
 901 the training set for 600 epochs using the Adam optimizer in Pytorch, with  $H = 1$ ,  $M = 5$ ,  $D = 5$ ,  
 902 batch size = 80. Learning rate was initialized to 0.01, and was decayed by a factor of 0.9 every 100  
 903 epochs.

910  
 911 A.3 ADDITIONAL DETAILS FOR STDP SIMULATION (SEC 3.2)

912 Our STDP simulation is largely based on [Neuromatch Academy \(2023\)](#). The dynamics of the LIF  
 913 neuron follows

$$914 \tau_m \frac{dV}{dt} = -(V - E_L) - g_E(t)(V - E_E) \tag{12}$$

$$915 V(t) \geq V_{th} \Rightarrow V(t) = V_{reset} \tag{13}$$

where  $V$  is the membrane potential,  $\tau_m$  is the membrane time constant,  $E_L$  is the resting potential,  $E_E$  is the synapse reversal potential,  $V_{th}$  is the spiking threshold, and  $V_{reset}$  is the reset potential. Once  $V(t)$  crosses the spiking threshold, we say the LIF neuron emits a spike, and  $V(t)$  will be reset to and held at  $V_{reset}$  for a refractory period  $t_{ref}$ .  $g_E(t)$  is the total excitatory synaptic conductance, which is the total conductance of all active pre-synapses (i.e. synapses coming into the LIF neuron) at that time:

$$g_E(t) = \sum_{i=1}^N g_i(t) \delta_i(t - t_{spk}) \quad (14)$$

where  $\delta_i$  is the delta function:  $\delta_i(t - t_{spk}) = 1$  if there is a spike at pre-synapse  $i$  at time  $t$ , and 0 otherwise. The conductance of each pre-synapse  $g_i$  evolves following

$$\frac{dg_i}{dt} = -\frac{g_i}{\tau_E} + \bar{g}_i \delta_i(t - t_{spk}) \quad (15)$$

where  $\tau_E$  is the EPSP time constant, and  $\bar{g}_i$  is the peak synaptic conductance of pre-synapse  $i$ . All  $\bar{g}_i$  are bounded between 0 and  $\bar{g}_{max}$ .

When there is a spike arriving at the  $i$ -th pre-synapse,

$$\bar{g}_i = \bar{g}_i + M(t) \bar{g}_{max} \quad (16)$$

where  $M(t)$  helps tracking the time since the last postsynaptic spike emitted by the LIF neuron. When the postsynaptic LIF neuron spikes, all pre-synapses are updated:

$$\bar{g}_i = \bar{g}_i + P_i(t) \bar{g}_{max}, \forall i \quad (17)$$

where  $P_i(t)$  helps tracking the time since the last spike at the  $i$ -th pre-synapse. STDP is enforced through  $M(t)$  and  $P_i(t)$ . Specifically,  $M(t)$  follows

$$\tau_- \frac{dM}{dt} = -M \quad (18)$$

and whenever the postsynaptic LIF neuron spikes,

$$M(t) = M(t) - A_- \quad (19)$$

$P_i(t)$  follows

$$\tau_+ \frac{dP}{dt} = -P \quad (20)$$

and whenever the  $i$ -th presynaptic neuron spikes,

$$P(t) = P(t) + A_+ \quad (21)$$

$\tau_+$  and  $\tau_-$  specify the range of separation between pre- and postsynaptic spikes where STDP takes effect.  $A_+$ ,  $A_-$  are both positive, and define the maximum amount of synaptic strengthening and weakening, respectively. It follows that  $M(t) \leq 0$ ,  $P_i(t) \geq 0 \forall t$ .  $M(t)$  and  $P_i(t)$  effectively capture the STDP rule

$$\Delta W = A_+ e^{(t_{pre} - t_{post})/\tau_+} \text{ if } t_{post} > t_{pre} \quad (22)$$

$$\Delta W = -A_- e^{-(t_{pre} - t_{post})/\tau_-} \text{ if } t_{post} < t_{pre} \quad (23)$$

as shown in Figure 3a. The constant parameters and initial conditions in our simulation are set in the same way as in [Neuromatch Academy \(2023\)](#), and are summarized in tables 2, 3. Pre-synaptic spike trains are modeled as independent Poisson processes with rate 50Hz.

To generate data, we run the simulation for 100,000 timesteps where each timestep corresponds to 1ms. We used the first 80% of data for training, and the last 20% of data as the test set. Membrane potential of the LIF neuron was then z-scored using its mean and std on the training set. We fitted 5 NetFormer models using different random seeds. All NetFormer models have  $H = 5$ ,  $M = 101$ ,  $D = 101$ , and were trained to minimize the mean squared error on the training set for 20 epochs using the Adam optimizer with learning rate 0.005, batch size 64 in Pytorch. Result from one seed is visualized in Figure 3d-f. We used a sliding window of length 10,000 timesteps to smooth both true and inferred synaptic weight trajectories before computing the correlation coefficients.

**Table 2:** Constant parameters in STDP simulation

Parameter	Value
$\tau_m$	10 [ms]
$E_L$	-75 [mV]
$E_E$	0 [mV]
$V_{th}$	-55 [mV]
$V_{reset}$	-75 [mV]
$t_{ref}$	2 [ms]
$\tau_E$	5 [ms]
$\bar{g}_{max}$	0.024
$\tau_+$	20 [ms]
$\tau_-$	20 [ms]
$A_+$	0.008
$A_-$	0.0088

**Table 3:** Initial conditions in STDP simulation

Variable	Initial value
$V$	-65 [mV]
$g_i$	0.014
$M$	0
$P$	0

#### A.4 ADDITIONAL DETAILS FOR TASK-DRIVEN POPULATION ACTIVITY SIMULATION

##### A.4.1 SIMULATION DETAILS

The hidden dynamics of RNN models follows equation 7, and at each timestep  $k$ , the network activity is read out through a linear mapping

$$\mathbf{y}_k = \mathbf{W}_{out} \mathbf{h}_k. \quad (24)$$

All RNN models are trained to minimize the cross entropy loss using the Adam optimizer in Pytorch. In the Perceptual Decision Making task, we trained a RNN with 4 hidden units for 5000 epochs using learning 0.005, batch size 32. In the Go-Nogo task, we trained a RNN with 8 hidden units for 2000 epochs using learning 0.01, batch size 32. In the Delay Comparison task, we trained a RNN with 12 hidden units for 5000 epochs using learning 0.01, batch size 32. All trained RNNs achieve over 90% accuracy in the 1000 test trials. All trials are generated using the default parameters in the NeuroGym toolkit (Molano-Mazon et al., 2022).

In each task, we recorded the hidden units activity of the trained RNN during the 1000 test trials. We then trained NetFormer to predict the next-step hidden units activity based on the present and past  $H$ -step hidden activity and stimulus inputs. Hidden units activity during 800 trials were used for training, and the remaining 200 trials were using for evaluation. In each task, we trained 5 NetFormer models from different initializations to minimize the mean squared error (MSE) on the training set using the Adam optimizer in Pytorch. In the Perceptual Decision Making task, NetFormer has  $H = 5$ ,  $N = M = D = 7$ , and was trained using learning rate 0.0025, batch size 64 for 100 epochs. In the Go-Nogo task, NetFormer has  $H = 1$ ,  $N = M = D = 11$ , and was trained using learning rate 0.01, batch size 64 for 50 epochs. In the Delay Comparison task, NetFormer has  $H = 5$ ,  $N = M = D = 14$ , and was trained using learning rate 0.005, batch size 64 for 50 epochs.

##### A.4.2 QUANTITATIVE COMPARISON WITH LINEAR REGRESSOIN MODEL

Table 4 provides a quantatitive comparison between NetFormer and the linear regression model.

	Dynamics prediction				Connectivity recovery			
	NetFormer		Linear		NetFormer		Linear	
	MSE	$R^2$	MSE	$R^2$	Spearman	Pearson	Spearman	Pearson
<b>a</b>	<b>0.000</b> $\pm$ 0.000	<b>0.998</b> $\pm$ 0.001	0.014	0.920	<b>0.694</b> $\pm$ 0.163	<b>0.760</b> $\pm$ 0.120	0.566	0.548
<b>b</b>	<b>0.010</b> $\pm$ 0.000	<b>0.972</b> $\pm$ 0.001	0.013	0.960	<b>0.622</b> $\pm$ 0.006	<b>0.722</b> $\pm$ 0.004	0.518	0.553
<b>c</b>	<b>0.001</b> $\pm$ 0.000	<b>0.997</b> $\pm$ 0.001	0.034	0.897	<b>0.811</b> $\pm$ 0.011	0.633 $\pm$ 0.105	0.626	<b>0.650</b>

**Table 4:** **a**, **b**, **c** corresponds to the Perceptual Decision Making task, Go-Nogo task, and Delay Comparison task, respectively. MSE and  $R^2$  were evaluated on concatenated held-out trials. Spearman and Pearson correlation coefficients were computed between the off-diagonal entries of the inferred and true connectivity matrices. NetFormer results are the mean $\pm$ std across 5 random seeds.

## A.5 CONNECTIVITY-CONSTRAINED SIMULATION AND NEURAL DATA: DATASETS AND PREPROCESSING

### A.5.1 CONNECTIVITY-CONSTRAINED SIMULATION

We used the following procedure to construct the ground-truth connectivity matrix. For each cell-type pair and for every pair of neurons, we first drew a random sample from the uniform distribution between 0 and 1. Then, we used the connectivity probability from patch-clamp experiments [Campagnola et al. \(2022\)](#) as a cutoff threshold to determine if two neurons are connected. For connected neurons, we sampled their connection strength from a normal distribution  $\mathcal{N}(\mu, 0.1)$ , where  $\mu$  is the measured post-synaptic potential from patch-clamp experiments. We simulated 30,000 steps for 200 neurons, using the first 80% timesteps for training and the last 20% for testing.

### A.5.2 PATCH-CLAMP DATASET

The dataset released in [Campagnola et al. \(2022\)](#) contains experimental results of connectivity probability and connectivity strength (Postsynaptic Potential (PSP)) at the cell-type level measured using patch-clamp. In each experiment, up to eight neurons were simultaneously subjected to whole-cell patch-clamp recording, mainly under current-clamp conditions, with some stimuli also tested under voltage-clamp conditions. Stimuli were applied to each patched neuron while recording the other neurons for postsynaptic responses. We mainly focus on the experimental results for layers 2/3 in mouse primary visual cortex (V1), to match the neurons recorded in the multimodal mouse dataset ([Bugeon et al., 2022](#)).

### A.5.3 MULTIMODAL MOUSE DATA

For functional activity recordings from neuronal populations, we used a recent, public multimodal dataset provided by [Bugeon et al. \(2022\)](#). This dataset includes spontaneous population activity recordings from the mouse primary visual cortex (V1) across layers 2/3 via 2-photon calcium imaging at a temporal sampling frequency of 4.3Hz across six 20-minute sessions, recording approximately 500 neurons per session. Spatial coordinates of the recorded neurons are also provided. We trained our models on data from one experimental subject (SB025), which includes recordings of 2481 neurons, with some neurons repeating across six sessions. The dataset also includes single-cell spatial transcriptomics, profiling mRNA expression for 72 selected genes to identify excitatory and inhibitory class labels of neurons. 51% of neurons in the inhibitory class can further be identified to be one of Lamp5, Pvalb, Vip, Sncg, and Sst.

### A.5.4 DATA PREPROCESSING

In the connectivity-constrained simulation, when using RNN with an exponential activation, we rescaled the data to ensure that all neuronal activities are nonnegative, as exponential activation produces only nonnegative outputs.

For the experimental neural recording, which is nonnegative, we normalized it using the mean and standard deviation calculated across all sessions and neurons involved in training. When using the RNN model with exponential activation, we normalized the data by dividing by the standard deviation only, without first subtracting the mean.

## 1080 A.6 BASELINES

### 1081 A.6.1 STATIONARY CONNECTIVITY BASELINES

1082 **Linear Regression:** We denote neural activity data as  $X_k = [x_{k-H+1} \cdots x_k] \in \mathbb{R}^{N \times H}$   
 1083 recorded from  $N$  neurons and  $H$  time steps. Let  $x_{k+1} \in \mathbb{R}^N$  denote the neuronal activity at the  
 1084  $(k+1)$ th time step. Given previous 1 time step,  $x_k$ , linear regression predicts current time step  
 1085 activity as  
 1086

$$1087 \hat{x}_{k+1} = Wx_k + b$$

1088 **Recurrent Neural Network (RNN) with tanh activation:** Given neuronal activity across previous  
 1089  $p$  time steps,  $x_k, x_{k-1}, \dots, x_{k-p+1}$ , a RNN with predefined Tanh activation function predicts current  
 1090 time step activity as  
 1091

$$1092 \hat{x}_{k+1} = \sigma \left( W^{(0)}x_k + W^{(1)}x_{k-1} + \cdots + W^{(p-1)}x_{k-p+1} + b \right), \sigma = \tanh$$

1093 where  $W^{(l)}, l \in \{0, 1, \dots, p-1\}$ , represent how the previous  $l$ -th step affects the current step activity  
 1094 and each element  $W_{ij}^{(l)}$  represents how the  $j$ -th neuron at the previous  $l$ -th time step influences the  
 1095  $i$ th neuron in current step. The RNN is trained by minimizing mean squared errors (MSE) of the  
 1096 current time step activity prediction given previous time steps.  $p = 1$  is commonly used for RNN.  
 1097 For modeling both simulation data and real mouse data, we chose  $p = 1$ , because the simulation data  
 1098 has exactly one timestep dependency. Using larger  $p$  did not improve performance in real data either.  
 1099

1100 **Recurrent Neural Network (RNN) with exponential activation:** Next, we change the predefined  
 1101 activation function of RNN to exponential function for modeling both simulation data and real mouse  
 1102 data.  
 1103

$$1104 \hat{x}_{k+1} = \sigma \left( W^{(0)}x_k + W^{(1)}x_{k-1} + \cdots + W^{(p-1)}x_{k-p+1} + b \right), \sigma = \exp$$

1105 **Cross correlation:** Recall that  $X_k = [x_{k-H+1} \cdots x_k] \in \mathbb{R}^{N \times H}$  denotes activity of  $N$  neurons  
 1106 across  $H$  time steps. Let  $x^{(i)}, x^{(j)} \in \mathbb{R}^H$  denote the  $i$ -th and  $j$ -th neurons' activity across  $H$  time  
 1107 steps. For simplicity, let  $a = x^{(i)}[\tau : ]$ ,  $b = x^{(j)}[: -\tau]$ . Cross correlation with time delay  $\tau$  reflects  
 1108 connectivity as  
 1109

$$1110 r^{i \leftarrow j} = \frac{a^\top b}{\|a - \bar{a}\| \|b - \bar{b}\|}$$

1111 We choose  $\tau = 1$  for inferring connectivity in both simulation and read data.  
 1112

1113 **Covariance:** Similar to above, let  $x^{(i)}, x^{(j)} \in \mathbb{R}^H$  denote the  $i$ -th and  $j$ -th neurons' activity across  
 1114  $H$  time steps. Covariance indicates the level to which two variables vary together. Covariance matrix  
 1115 is symmetric, which assumes that the influence from neuron  $i$  to neuron  $j$  is the same as influence  
 1116 from neuron  $j$  to neuron  $i$ . Covariance between neuron  $i$  and  $j$  is defined as  
 1117

$$1118 c^{i \leftarrow j} = c^{j \leftarrow i} = \frac{1}{H-1} \sum_{k=1}^H x_k^{(i)} x_k^{(j)}$$

1119 **Mutual information:** Mutual information quantifies the amount of information that one random  
 1120 variable contains about another, which is also symmetric. When calculating the mutual information  
 1121 between activity history of two neurons, the computation involves estimating the entropy of each  
 1122 neuron's activity individually and the joint entropy of both neurons together. We used the Python  
 1123 package PyInform.mutualinfo to compute the mutual information. Let  $x^{(i)}, x^{(j)} \in \mathbb{R}^H$  as defined  
 1124 above, then  
 1125

$$1126 I^{i \leftarrow j} = I^{j \leftarrow i} = I(x^{(i)}; x^{(j)}) = H(x^{(i)}) + H(x^{(j)}) - H(x^{(i)}, x^{(j)}),$$

1127 where  $H(x^{(i)})$  is the entropy of neuron  $i$ 's activity, calculated as  $H(x^{(i)}) = -\sum_{z \in x^{(i)}} p(z) \log p(z)$ .  
 1128  $H(x^{(j)})$  is the entropy of neuron  $j$ 's activity.  $H(x^{(i)}, x^{(j)})$  is the joint entropy of neurons  $i$  and  $j$ ,  
 1129 calculated as  $H(x^{(i)}, x^{(j)}) = -\sum_{z \in x^{(i)}, \xi \in x^{(j)}} p(z, \xi) \log p(z, \xi)$ .  
 1130

1131 **Transfer entropy:** Transfer entropy quantifies the amount of directed information transferred  
 1132 between systems, or in our case, between two neurons. We used the Python package PyIn-  
 1133

form. transfer entropy to compute the transfer entropy, which is defined as

$$T^{i \leftarrow j} = \sum p \left( x_{k+1}^{(i)}, x_{(k+1-p):k}^{(i)}, x_{(k+1-l):k}^{(j)} \right) \log \left( \frac{p \left( x_{k+1}^{(i)} \mid x_{(k+1-p):k}^{(i)}, x_{(k+1-l):k}^{(j)} \right)}{p \left( x_{k+1}^{(i)} \mid x_{(k+1-p):k}^{(i)} \right)} \right),$$

where  $x_{k+1}^{(i)}$  is the future activity of neuron  $i$ .  $x_{(k+1-p):k}^{(i)}$  represents the past  $p$  activities of neuron  $i$  up to time  $k$ .  $x_{(k+1-l):k}^{(j)}$  denotes the past  $l$  activities of neuron  $j$  up to time  $k$ .  $p(\cdot)$  denotes the probability distributions calculated from the joint and conditional activities as observed in the data.

## A.6.2 NONSTATIONARY CONNECTIVITY BASELINES FOR NEURAL DATA

**Low-tensor-rank RNN (LtrRNN):** LtrRNN is designed to model trial-varying neural dynamics by capturing low-dimensional changes in connectivity over time. We split continuous neural activity data into overlapping sliding windows, treating each window as a distinct trial, which allows LtrRNN to learn temporal variations in connectivity patterns. The dimension of the network is defined by the number of neurons. By extracting the trial-specific weight matrices from LtrRNN, we compared these non-stationary connectivity patterns with the attention maps learned by NetFormer. Code for fitting LtrRNN: <https://github.com/arthur-pe/LtrRNN>

**Autoregressive Hidden Markov Model (AR-HMM):** AR-HMM extends the traditional HMM by incorporating state-specific autoregressive dynamics, where each state has its own unique autoregressive model to describe the temporal dynamics of neural activity. AR-HMM is able to infer the latent states of the system and estimates the connectivity matrices associated with each state. However, a limitation of AR-HMM is the need to predefine the total number of states. Code for fitting AR-HMM: <https://github.com/lindermanlab/ssm>

## A.7 MORE ON CONNECTIVITY-CONSTRAINED SIMULATION

### A.7.1 CONNECTIVITY-CONSTRAINED SIMULATION WITH SIGMOID NONLINEARITY

To test the robustness of NetFormer towards different nonlinear activations in the connectivity-constrained simulation described in Section 4, we replaced the tanh activation with sigmoid activation and used NetFormer, along with other baselines, to reconstruct connectivity at both neuron-level and cell-type level. Table 5 presents quantitative comparisons of the inferred connectivity with ground truth, averaged over five random seeds. Both Table 5 and Figure 11 demonstrate that NetFormer outperforms the other baselines on neuron-level ( $N \times N$ ) connectivity inference.

		NetFormer	linear regression	RNN w/ tanh	RNN w/ exp	cross correlation	covariance	mutual information	transfer entropy	
simulation	connectivity	Pearson	<b>0.834</b> ±0.006	0.765±0.002	0.772±0.001	0.679±0.002	0.829	-0.022	0.447	0.329
	$N \times N$	Spearman	<b>0.508</b> ±0.005	0.482±0.002	0.485±0.001	0.454±0.000	0.512	-0.006	0.201	0.223
	connectivity	Pearson	0.880±0.003	0.904±0.002	<b>0.940</b> ±0.001	0.803±0.002	0.921	-0.438	0.350	0.304
	$K \times K$	Spearman	0.860±0.002	0.862±0.003	<b>0.886</b> ±0.000	0.788±0.011	0.856	-0.299	0.104	0.340

**Table 5: Connectivity-constrained simulation with sigmoid activation.** Results of connectivity inference using mutual information, transfer entropy, and Granger causality are assessed by comparing against the absolute values of ground truth connectivity. Simulation data has ground truth for both neuron-level ( $N \times N$ ) and cell type-level ( $K \times K$ ) connectivities. Connectivity inference is assessed using Spearman’s and Pearson’s correlation coefficients.

### A.7.2 GRANGER CAUSALITY TEST

We performed Granger causality tests on connectivity-constrained simulation data with both sigmoid and tanh activations. To create a binary ground-truth neuron-level connectivity matrix, we assigned a value of 1 to all nonzero entries and 0 to zero entries. We then conducted Granger causality tests on pairwise neural activities to generate a matrix of test statistics, which is then min-max normalized. To compare with Granger causality on inferring binary connectivity, we also performed min-max normalization on the time-averaged neuron-level attention matrix. We evaluated the performance

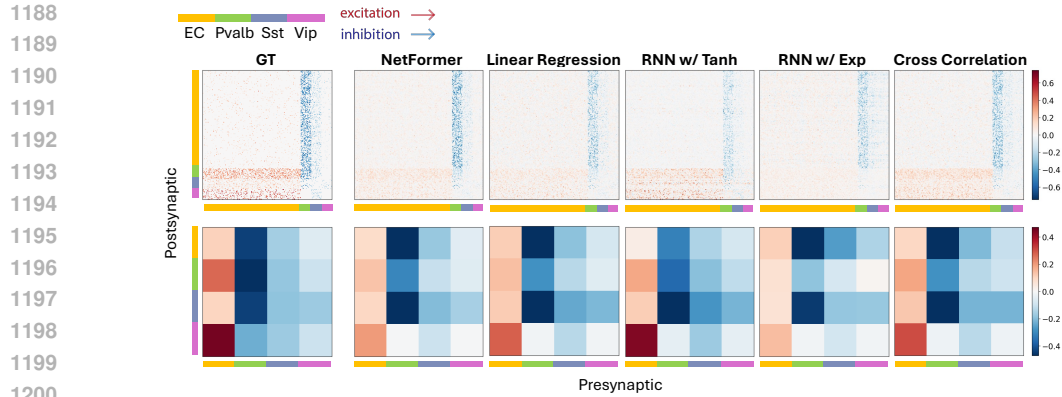


**Figure 11: Connectivity-constrained simulation with sigmoid activation.** Visualization of ground truth and inferred connectivity matrices at both individual-neuron level and cell-type level. A positive linear transformation has been applied to standardize all matrices to the same range for better visualization.

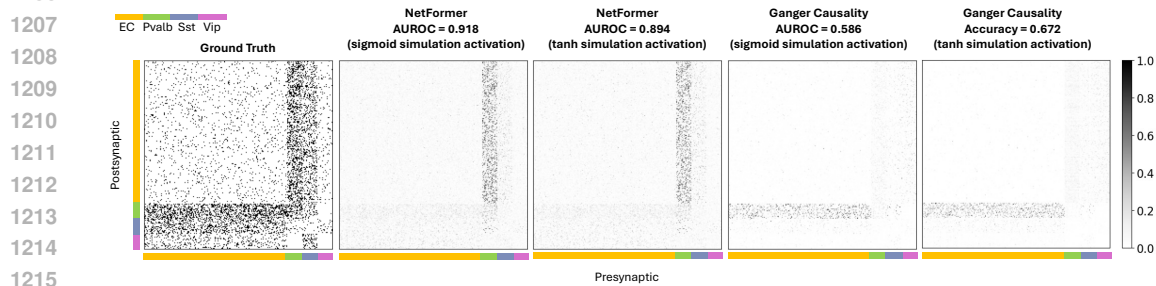


**Figure 12:** Visualization of NetFormer and Granger causality results for inferring binary connectivity (presence or absence of connections) in connectivity-constrained simulation data.

using AUROC. As shown in Figure 12, for simulations with sigmoid activation, the AUROC of NetFormer is 0.918, while the AUROC of Granger causality is 0.586. For simulations with tanh activation, the AUROC of NetFormer is 0.894, while the AUROC of Granger causality is 0.672. On both simulations, NetFormer shows better performance

#### A.8 NETFORMER FOR NONSTATIONARY CONNECTIVITY INFERENCE ON NEURAL DATA

We visualized neural activity traces, mouse behavioral states, and cell-type level attention weights for each state in Figure 13. While behavioral states are not provided as model inputs, they can be inferred using unsupervised methods such as PCA or clustering on NetFormer’s attention weights. Figure 13a shows that NetFormer predictions effectively capture overall patterns of neural activity. Figure 13b shows that intra-state connectivity is more consistent compared to connectivity across different states.

We also benchmarked NetFormer with LtrRNN and AR-HMM on state-dependent connectivity inference, as shown in Table 6. We compared the inferred connectivity with the patch-clamp experimental result.

#### A.9 NETFORMER APPLIED TO NETWORKS WITH SPURIOUS CORRELATIONS

Das & Fiete (2020) shows that connectivity inference can be obscured by spurious correlations arising from strong recurrent connections. To assess NetFormer’s resilience to such spurious correlations, we performed two experiments on simulated neuron populations with strong recurrent connections. In the first experiment, we generated continuous activity from the simulated network, where NetFormer is directly applicable. In the second experiment, we generated spiking activity from the simulated

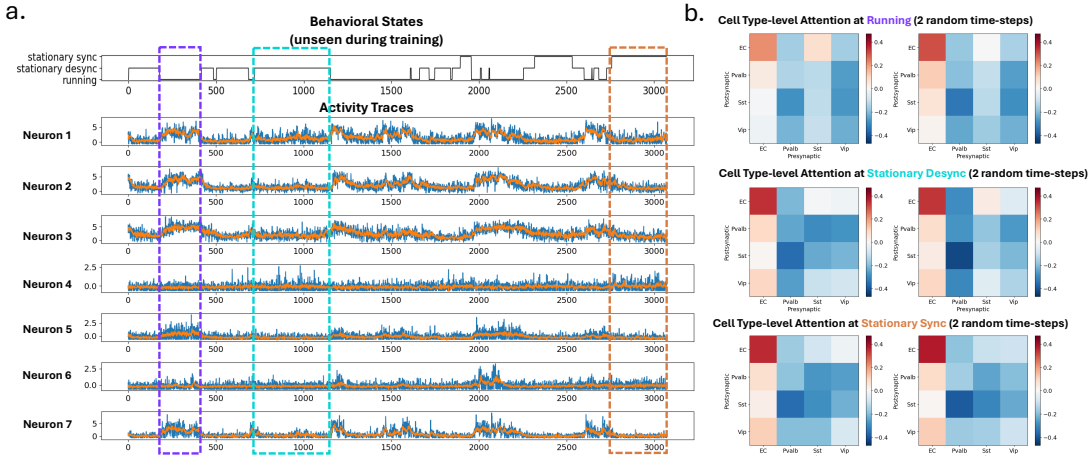


**Figure 13:** **a.** Visualization of neural data and behavioral states for an example session. Top row: behavioral states. Predicted activity traces from NetFormer are shown in orange, while measured activity traces are shown in blue. **b.** Three blocks of time from **a.** are selected, and each represents a different state. Two timesteps within each block are randomly selected to showcase the change of attention weights within states and between states.

			NetFormer	LtrRNN	AR-HMM
in-vivo recording	Running K × K	Pearson	0.591±0.204	0.007±0.182	0.199±0.027
		Spearman	0.601±0.209	-0.036±0.189	0.274±0.048
	Stationary Desync K × K	Pearson	0.662±0.176	-0.003±0.181	-0.320±0.012
		Spearman	0.723±0.173	-0.057±0.174	-0.206±0.017
	Stationary Sync K × K	Pearson	0.713±0.148	0.000±0.186	0.145±0.041
		Spearman	0.767±0.151	0.069±0.175	0.151±0.009

**Table 6: State-dependent connectivity inference.** NetFormer attentions and LtrRNN weight matrices are grouped by state labels and averaged for each state. The inferred connectivity for each state is compared against Postsynaptic Potential (PSP) resting state amplitude obtained from patch-clamp experiments.

network, which follows Das & Fiete (2020) more closely but requires modifying the objective function of NetFormer. In both experiments, we simulated neuron populations of size 100. The population connectivity matrices in both experiments are constructed in the same way as Das & Fiete (2020) with a local Mexican hat profile. Specifically, the connection weight between neurons  $i$  and  $j$  is computed as

$$w_{ij} = e^{-d_{ij}^2/2\sigma_1^2} - ae^{-d_{ij}^2/2\sigma_2^2}, \tag{25}$$

where  $d_{ij}$  is the distance between neurons  $i$  and  $j$  (in units of neurons),  $\sigma_1 = 6.98$ ,  $\sigma_2 = 7$ , and  $a = 1.0005$ .

### A.9.1 NETWORK WITH CONTINUOUS ACTIVITY

The network model used to generate the data is similar to equation 9, with modifications to the feed-forward inputs  $b$  and incorporation of the recurrent weight strength  $r$ . Specifically, Gaussian noise is injected into the feed-forward inputs to mimic the simulation network described in Das & Fiete (2020).

$$\mathbf{x}_{k+1} = \tanh(r\mathbf{W}\mathbf{x}_k + \mathbf{b}(1 + \epsilon_k)). \tag{26}$$

We conducted similar experiments as in Das & Fiete (2020) by varying the recurrent weight strength  $r$ . The corresponding connectivity inference results are shown in Figure 14. When the recurrent weight strength is large (e.g.  $r = 35$ ), spurious correlations between neurons appear, as seen in the synchronized activity and noise correlation. On the other hand, when the recurrent weight strength is



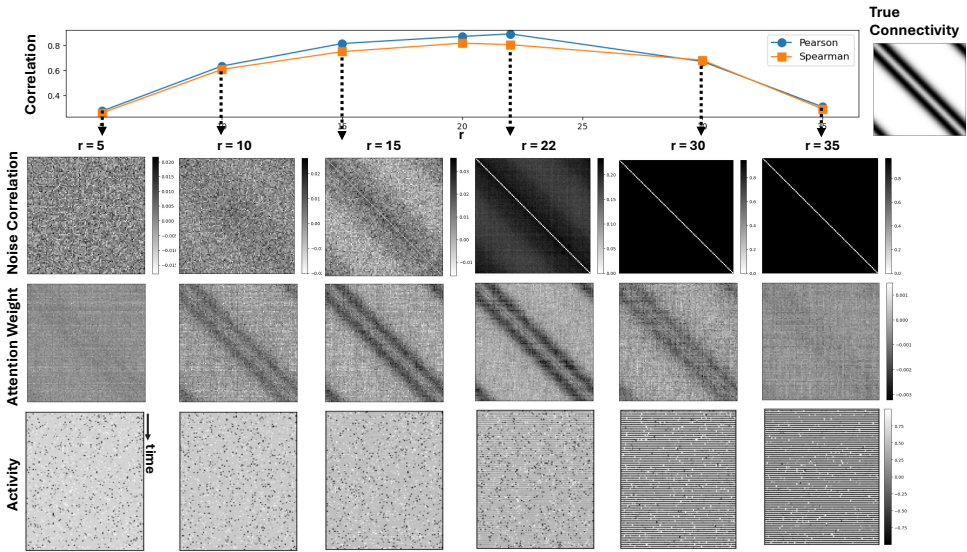


**Figure 14: Connectivity-constrained simulation with ring circuit connectivity.** Correlation between attention weight as connectivity inference and ground-truth recurrent weights (top row), noise correlations (second row), attention weights (third row), and time-by-neuron activity traces (last row), at different recurrent weight strengths  $r$ .

small (e.g.  $r = 5$ ), activity is mainly driven by noise rather than recurrent connections, making it hard to infer connectivity by fitting activity. In both extremes, NetFormer will struggle to capture the underlying ground-truth connectivity, as reflected by lower correlations with the ground truth. That being said, NetFormer still recovers some patterns of the ground truth, better than what noise correlation alone can capture.

### A.9.2 NETWORK WITH SPIKING ACTIVITY

To adapt NetFormer for modeling spiking activity, we take the exponential of NetFormer’s output as the mean rate of the Poisson distribution for spike generation. The spike generation process is constructed in the same way as Das & Fiete (2020), which we describe briefly below, and we refer the readers to the original paper for more details.

Let  $s_k, g_k, \sigma_k$  denote the synaptic activation, neural input, and emitted spikes of the neuron population at timestep  $k$ , respectively.  $g_k$  includes both inputs from other neurons and externally injected inputs  $b_k$ ; that is,

$$g_k = rW s_k + b_k. \tag{27}$$

At timestep  $k$ , the  $i$ -th neuron will emit a spike, that is,  $\sigma_k^{(i)} = 1$ , if the input it receives exceeds a certain threshold, that is,  $g_k^{(i)} > \Theta$ .

To fit the NetFormer, at every timestep  $k$ , we have

$$\hat{g}_k = \text{NetFormer}(s_k, \dots, s_{k-H+1}), \tag{28}$$

$$\hat{\lambda}_k = \exp(\hat{g}_k), \tag{29}$$

$$\hat{\sigma}_k \sim \text{Poisson}(\hat{\lambda}_k). \tag{30}$$

This setup is chosen to match the setup for GLM in Das & Fiete (2020) (see Equation 9 there). One minor difference is that, as model inputs, they used past spike trains convolved with a decaying exponential kernel, while we used the synaptic activation. Nonetheless, since their filter is truncated at a value much larger than the exponential decay time constant, it can be easily verified that these are actually very similar.

We followed the procedure described in Das & Fiete (2020) to generate population activity at different recurrent strength  $r$ . We followed the data generation code provided by the authors

at [https://github.com/FieteLab/neural-circuit-inference/blob/main/riken\\_demo.m](https://github.com/FieteLab/neural-circuit-inference/blob/main/riken_demo.m). We adopted  $r$  and spiking thresholds listed in [https://github.com/FieteLab/neural-circuit-inference/blob/main/thresholds\\_pinned.mat](https://github.com/FieteLab/neural-circuit-inference/blob/main/thresholds_pinned.mat). After the simulation starts, we collected activity after the initial 10,000 simulation timesteps in order for the network activity to stabilize. A total of 100,000 timesteps were collected, where the first 80,000 steps were used as the training set, and the rest 20,000 steps were used as the test set. Since this is a prototype study, the data volume we used here is much smaller than what is used in the original paper: their experiments are typically done on  $10^8$  spikes, while there are on average  $5.05 \times 10^4$  spikes in our training set across all  $r$ . Nevertheless, synchronized activity patterns and high noise correlation at large  $r$  can also be observed in our training set (Figure 15).

For all  $r$ , we used NetFormer with  $H = 1, N = 100, D = 100$ . For  $r = 0.0225, M = 40$ , and  $M = 100$  for the rest of  $r$ . All NetFormer models were trained to minimize the negative Poisson log likelihood loss on the training set, using batch size 32 for 100 epochs. We used learning rate 0.001 for  $r = 0.0025, 0.005, 0.002$  for  $r = 0.0075, 0.01, 0.0125, 0.015, 0.0175, 0.02, 0.025$ , and 0.0005 for  $r = 0.0225$ . We used the average NetFormer attention across test set timesteps as the NetFormer-inferred connectivity. Each row in NetFormer-inferred connectivity is then rescaled to minimize the  $l_2$  distance from the corresponding row in the ground-truth connectivity matrix, as also done in Das & Fiete (2020). Visually, Figure 15 shows that NetFormer-inferred connectivity can be affected by the presence of strong spurious correlation in neural activity, while being more resilient than noise correlation. Quantitatively, we computed the Spearman and Pearson correlation coefficients between the off-diagonal entries of NetFormer-inferred connectivity and true connectivity. We also computed the inference error (the  $l_2$  distance between the off-diagonal entries of true and inferred connectivity weights) as in Das & Fiete (2020). Consistent with their findings in Figures 2 and 3, we observe a U-shape curve in inference error as a function of  $r$ , and an inverted U-shape curve for correlation.

## A.10 IMPLEMENTAION DETAILS

### A.10.1 MODEL FRAMEWORK FOR FITTING CONNECTIVITY-CONSTRAINED SIMULATION AND REAL MOUSE DATA

Following Section 2, we train the NetFormer to predict  $x_{k+1}$  based on  $X_k = [x_{k-H+1} \cdots x_k] \in \mathbb{R}^{N \times H}$ . To encode neuron identities, a learnable positional embedding matrix  $E \in \mathbb{R}^{N \times M}$  is concatenated to  $X$ , giving  $\tilde{X}_k = [X_k \ E] \in \mathbb{R}^{N \times (H+M)}$ . The queries  $Q_k$  and keys  $K_k$  are obtained through linear transformations of  $\tilde{X}_k$ ,  $Q_k = \tilde{X}_k W_Q \in \mathbb{R}^{N \times D}$ , and  $K_k = \tilde{X}_k W_K \in \mathbb{R}^{N \times D}$ . NetFormer model is trained to predict the next time-step activity  $x_{k+1}$ , defined as

$$\hat{x}_{k+1} = A_k x_k + x_k = \phi\left(\frac{Q_k K_k^T}{\sqrt{D}}\right) x_k + x_k = \frac{1}{\sqrt{D}} (\tilde{X}_k W_Q) (W_K^T \tilde{X}_k^T) x_k + x_k,$$

where  $A_k$  is the self-attention that we want to use for inferring connectivity,  $\phi$  is the attention activation. In the standard Transformer model Vaswani et al. (2017), softmax is used as the attention activation function, but here we set  $\phi$  equal to identity for better interpretability. In fact, we experimented with different activation functions and empirically found that the identity activation yields the best results on recordings from the mouse cortex.

Although not used in the current experiments, it is possible to use an additional linear transformation on  $\hat{X}_k$  to accommodate neuronal dynamics that can depend on multiple previous timesteps, that is,

$$\hat{x}_{k+1} = A_k (X_k w_{out}) + X_k w_{out}, w_{out} \in \mathbb{R}^{H \times 1}.$$

### A.10.2 NETFORMER TRAINING AND EVALUATION

We first assign each unique neuron across all sessions an ID, which is later used to track positional embedding for each unique neuron, because same neuron can be recorded in more than one session. Then, within each session, we construct samples with window size 200 in simulation and 60 in real data, and we make sure samples in one batch should come from the same session so that the dimensions can match.

We use the first 80% timesteps in all sessions for training and the last 20% timesteps for validation. The model is trained using MSE as the loss function, comparing the predicted activity for the next

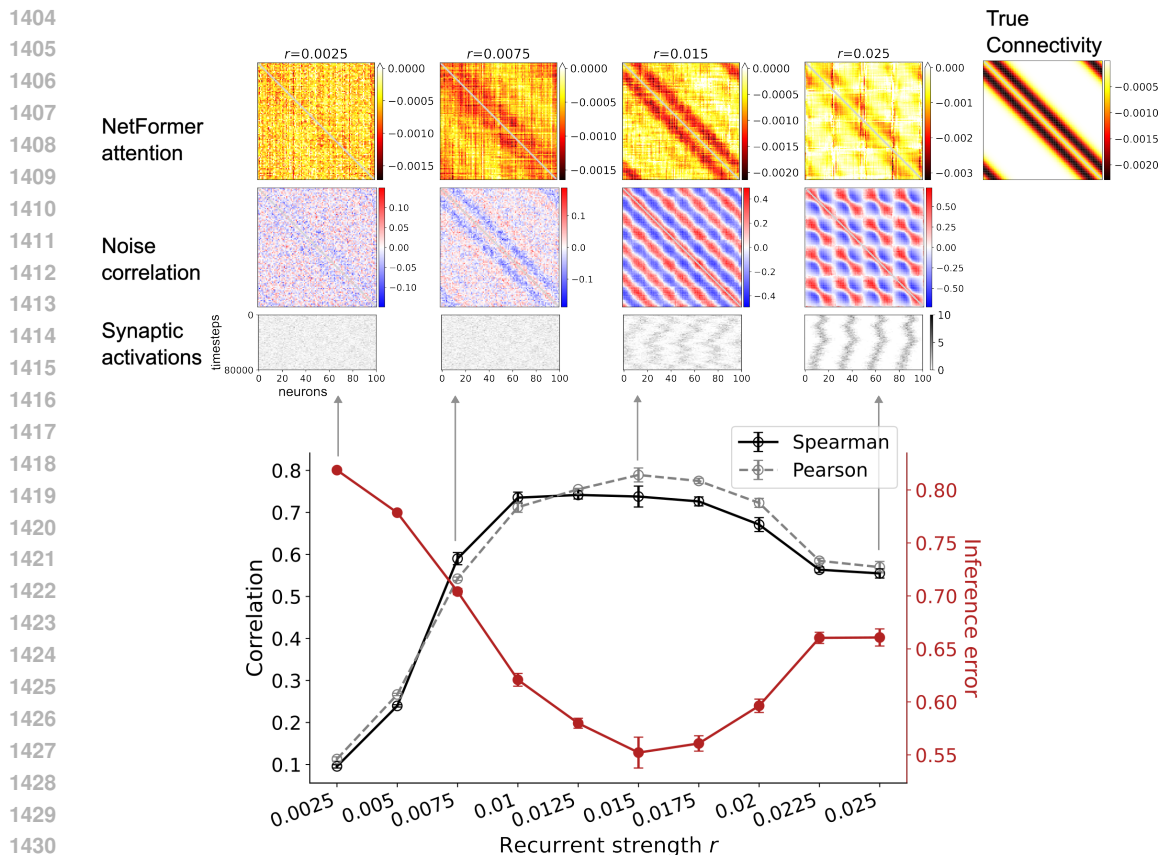


**Figure 15: NetFormer for spiking neuron population.** Correlation and inference error between true and NetFormer-inferred connectivities. Errorbars: mean $\pm$ std across three random initializations for NetFormer. In addition, rescaled NetFormer-inferred connectivity, noise correlation, and population synaptic activations at four example  $r$  are visualized. For correlation and connectivity matrices, colorbars indicate the scale of the off-diagonal entries, and the diagonal entries are masked in grey.

time step with the ground-truth activity. We employ early stopping criteria, ceasing training if there are 20 epochs without improvement, with a hard limit of 100 epochs maximum.

After training is complete, we calculate the attention for each sample in the dataset. For each session, we aggregate the attentions from all samples to compute a single time-averaged attention. Averaged attentions from all sessions are then transformed into a final cell-type level attention. We achieve this by aggregating attention values according to their corresponding presynaptic and postsynaptic cell types and dividing by the total count of such pairs.

We also extract positional embeddings from the trained model and utilize each neuron’s unique ID to determine the neuronal embedding for every unique neuron. These embeddings are then used as features for logistic regression to classify neurons as either excitatory or inhibitory (Figure 5b).

For evaluation, we assess the inferred cell-type level connectivity against the Postsynaptic Potential (PSP) resting state amplitude obtained from patch-clamp experiments, which serves as the experimental ground-truth. Additionally, we evaluate the accuracy of the binary cell-type classification using experimental data from single-cell spatial transcriptomics, which provides a classification of neurons into excitatory and inhibitory types across all sessions.

### A.10.3 EVALUATION METRICS

We use python libraries and built-in functions for computing evaluation metrics.

1458 For connectivity inference, we flatten the inferred 2-dimensional  $N \times N$  or  $K \times K$  connectivity  
1459 matrix and ground-truth matrix.

1460 **Pearson correlation:** `scipy.stats.pearsonr()`

1461 **Spearman rank correlation:** `scipy.stats.spearmanr()`.

1462 For activity prediction, given the input matrix  $\in \mathbb{R}^{B \times N \times H}$  for NetFormer and input matrix  $\in \mathbb{R}^{B \times N}$   
1463 for RNN, where  $B$  is the batch size, NetFormer outputs  $\in \mathbb{R}^{B \times N \times 1}$  and RNN outputs  $\in \mathbb{R}^{B \times N}$ . We  
1464 flatten the predicted activity and the ground-truth.

1465 **MSE:** `torch.nn.functional.mse_loss()`

1466 **Pearson correlation:** `scipy.stats.pearsonr()`

1467 **R<sup>2</sup>:** `sklearn.metrics.r2_score()`

1468 For binary classification, classifier predicts the probability for all neurons.

1469 **Top-1 accuracy:** `sklearn.metrics.accuracy_score()`

1470 **Area Under the Receiver Operating Characteristic (AUROC):** `sklearn.metrics.roc_auc_score()`

1471

#### 1472 A.10.4 HYPERPARAMETERS

1473

1474 In connectivity-constrained simulation data, for training NetFormer, we use history window size 100,  
1475 embedding size 200, hidden dimension of query and key matrices is 300, learning rate  $10^{-3}$ , and  
1476 batch size 32. For training RNN, we use  $p = 1$ , batch size 32, and learning rate  $10^{-3}$ .

1477 In real data, for training NetFormer, we use history window size 60, embedding size 30, hidden  
1478 dimension of query and key matrices 90, learning rate  $10^{-3}$ , and batch size 32. For training RNN,  
1479 we use  $p = 1$ , batch size 32, and learning rate  $10^{-4}$ .

1480 We use PyTorch [Paszke et al. \(2017\)](#) and PyTorch Lightning [Falcon & The PyTorch Lightning team](#)  
1481 [\(2019\)](#) for model development and training, and Adam as the optimizer.

1482

#### 1483 A.10.5 PSEUDO CODE

1484

1485 We train NetFormer and extract attentions and positional embeddings for connectivity inference  
1486 and binary cell-type classification. The pseudo code for model training, connectivity inference and  
1487 cell-type classification is provided as follows:

1488

```
1489 NetFormer(x, neuron_ids):
1490     if constraint == True:
1491         cell_type_level_mean = parameters(num_cell_type, num_cell_type)
1492         cell_type_level_var = parameters(num_cell_type, num_cell_type)
1493
1494     embeddings = embedding_table(neuron_ids)
1495     input = layer_norm(concat(x, embeddings))
1496     x, embeddings = input[:, :, :T], input[:, :, T:]
1497
1498     dim_x, dim_e = x.shape[-1], embeddings.shape[-1]
1499     scale = (dim_x + dim_e) ** -0.5
1500
1501     logits = input @ W_Q_W_KT @ input.T
1502     logits = logits * scale
1503
1504     if activation == softmax:
1505         attention = softmax(logits)
1506     elif activation == sigmoid:
1507         attention = sigmoid(logits)
1508     elif activation == tanh:
1509         attention = tanh(logits)
1510     elif activation == none:
1511         attention = logits
1512
1513     output = layer_norm(attention @ x + x)
```

```

1512     if out_layer == True:
1513         # linear_out is a linear transformation from dimension T to 1
1514         output = linear_out(output)
1515         return output, attention
1516     else:
1517         # Use the last column as prediction
1518         return output[:, :, -1], attention
1519
1520 NetFormer_Training(all_samples):
1521     all_inputs, all_neuron_ids, all_GT_targets = all_samples
1522     model = NetFormer()
1523     optimizer = Adam(model, learning_rate)
1524
1525     all_predictions, all_attentions = model(all_inputs, all_neuron_ids)
1526
1527     prediction_loss = MSE(all_predictions, all_GT_targets)
1528     loss = prediction_loss
1529
1530     optimizer.zero_grad()
1531     loss.backward()
1532     optimizer.step()
1533
1534 Connectivity_Inference(all_samples, trained_NetFormer, GT_connectivity):
1535     all_inputs, all_neuron_ids, all_GT_targets = all_samples
1536     all_predictions, all_attentions = trained_NetFormer(all_inputs, all_neuron_ids)
1537
1538     avg_attention = mean(all_attentions, axis=0)
1539
1540     pearson_corr = pearsonr(GT_connectivity, avg_attention)
1541     spearman_corr = spearmanr(GT_connectivity, avg_attention)
1542
1543 Cell_Type_Classification(trained_NetFormer, neuron_ids, cell_types):
1544     embeddings = trained_NetFormer.embedding_table(neuron_ids)
1545
1546     X_train = embeddings[TRAIN_idx]
1547     y_train = cell_types[TRAIN_idx]
1548     X_test = embeddings[TEST_idx]
1549     y_test = cell_types[TEST_idx]
1550
1551     # Train classifier
1552     classifier = LogisticRegression.fit(X_train, y_train)
1553     # Test on test set
1554     y_pred = classifier.predict(X_test)

```

## 1555 A.11 COMPUTE RESOURCES

1557 Model training on simulated systems in Section 3 was done on a MacBook Pro with Apple M1 chip.  
1558 Using the NVIDIA A100 GPU, NetFormer model trained on connectivity-constrained simulation  
1559 data took about 10min. NetFormer model trained on one mouse (SB025) in real mouse data took  
1560 about 20min, which requires at least 30 GB of RAM and 16 GB of GPU memory.

1561  
1562  
1563  
1564  
1565